Theses and Dissertations

August 2013

Effect of Relative Humidity in High Temperature Oxidation of Ceria Nanoparticles Coating on 316L Austenitic Stainless Steel

Luis Giraldez Pizarro
University of Wisconsin-Milwaukee

EFFECT OF RELATIVE HUMIDITY IN HIGH TEMPERATURE OXIDATION OF CERIA NANOPARTICLES COATING ON 316L AUSTENITIC STAINLESS STEEL

by

Luis Miguel Giraldez Pizarro

A Thesis Submitted in

Partial Fulfillment of the

Requirements for the Degree of

Master of Science

in Engineering

at

The University of Wisconsin-Milwaukee

August 2013

ABSTRACT
EFFECT OF RELATIVE HUMIDITY IN HIGH TEMPERATURE OXIDATION OF CERIA NANOPARTICLES COATING ON 316L AUSTENITIC STAINLESS STEEL

by

Luis Miguel Giraldéz Pizarro

The University of Wisconsin-Milwaukee, 2013
Under the Supervision of Professor Benjamin Church

A solution of 20 wt. % colloidal dispersion of Cerium Oxide (CeO_2) in 2.5% of acetic acid, was used for depositing a coating film on an austenitic stainless steel 316L. Cerium compounds have been distinguished as potential corrosion inhibitors in coatings over several alloys. The oxidation behavior of the cerium oxide coating on 316L austenitic stainless steel alloy was evaluated in dry and humid environments, the weight changes ($\Delta W/A$) was monitored as a function of time using a custom built Thermogravimetrical Analysis (TGA) instrument at temperatures of 750℃, 800℃ and 850℃, and different relative humidity levels (0%, 10% and 20%) respectively.   The parabolic oxidation rate and activation energy is calculated experimentally for each relative humidity level.

A measurement of the effective diameter size of the ceria nanoparticles was performed using a Light Scattering technique.   A characterization of the film

morphology and thickness before the oxidation was executed using Atomic Force Microscopy (AFM)

Microstructure and chemical composition of the oxidized coated substrates were analyzed using Scanning Electronic Microscopy (SEM) with energy dispersive spectroscopy (EDS). X-Ray Diffractometer (XRD) was used to characterize oxides formed in the surface upon isothermal treatment. A comparison of activation energy values obtained to identify the influence of relative humidity in the oxidation process at high temperature was conducted.

Cerium oxides coating may prevent crevice corrosion and increase pitting resistance of 316L relative to the uncoated substrate at high temperatures and different levels of relative humidity acting as a protective oxidation barrier.

The calculated parabolic rate constants, kp, at the experimental temperatures tend to increase as a function of humidity levels. The activation energy tends to increase proportionally to higher level of humidity exposures.

At 0% relative humidity a value of 319.29 KJ/mol of activation energy is being obtained and at 20% is 366.10 KJ/mol. For the 10% an approximate value of 343.00 KJ/mol has been estimated based on the projection of the kp values at 750°C and 800°C.

The presence of the CeO_2 coating film, reduced the oxidation kinetics and provided good cyclic oxidation resistance at increments of relative humidity.

TABLE OF CONTENTS

LIST OF FIGURES

LIST OF TABLES

ACKNOWLEDGEMENTS

"It is not the destination, but the journey that matters most..."

1.   INTRODUCTION

The use of rare earth metals such as Cerium as coatings to improve the protection of structural materials against oxidation at elevated temperature have attracted significant attention in recent years. Oxides inert to substrates may be used in coatings as a physical barrier to oxygen.

High temperature oxidation materials such as the austenitic stainless steel 316L, is known to exhibit good corrosion and oxidation resisting qualities. Cerium oxide coatings on stainless steels reverses the diffusion mechanism from iron outward diffusion to oxygen inward diffusion, due to that the energy barrier of Iron diffusion through cerium doped chromium is higher than that of oxygen diffusion. Cerium oxide has shown unique properties as oxygen storage, and in high temperature oxidation resistance for different alloys [1].

However, the different atmospheric conditions where different alloys are exposed and in this case an austenitic stainless steel have been performing, requires additional consideration such as the addition of cerium oxide coating to improve the corrosion and oxidation properties; and the impact of relative humidity on different levels. Improvements to the oxidation resistance of austenitic stainless steels would be an obvious benefit to many modern applications where high temperature durability is a concern. Still, it is important to understand and attempt to quantify benefits provided by a strategy such as cerium oxide coatings

This research presents an experimental case under controlled atmospheric conditions (relative humidity and temperature) and the oxidation response of the substrate with a cerium oxide coating applied. For this purpose a series of coated samples through a spraying method has been oxidized at high temperatures and different levels of relative humidity. The performance of the oxidation protection is evaluated.

Cerium oxide has been widely investigated because of its multiple applications, such as a catalyst, an electrolyte material of solid oxide fuel cells, a material of high refractive index, and an insulating layer on silicon substrates [2]

2. BACKGROUND

2.1   High Temperature Oxidation

Under most conditions high-temperature oxidation of metals results in the formation of an oxide film or scale on the metal surface; oxide layers thinner than 3000A are called films and thicker than 3000A are called scales.   The mechanism of oxidation depends on the nature of the scale, that is, whether the oxide is solid or liquid or if it also partially evaporates. If solid scales are formed, the oxidation behavior also depends on whether the scales are compact or porous.

A compact scale acts as a barrier which separates the metal and the oxygen gas. If sufficient oxygen is available at the oxide surface, the rate of oxidation at high temperatures will be limited by a solid-state diffusion, for example, lattice, grain boundary, or short-circuit diffusion, through the compact scale. As the diffusion distance increases as the oxide grows in thickness, the rate of reaction will decrease with time. Compact scales and films offer the best protective properties, and from a practical point of view they are the most important feature of oxidation of metals.   In all attempts to improve the oxidation resistance of metals and alloys, the goal is to improve the protective properties of the oxide film [3].

2.2.   Oxidation Kinetics

Metals are thermodynamically unstable with respect to their oxides over such a broad range of temperatures and oxygen pressures that the widespread use of metals (or metallic materials in general) as structural materials would be precluded except for the intervention of chemical kinetics. Fortunately, once an oxide has formed on the surface of a metallic material, it acts as a barrier to further reaction by mechanically separating the two reactants. Oxidation can then proceed only by transport of metal atoms to the oxide-ambient interface, by transport of oxygen atoms to the oxide-metal interface, or by breakage or physical removal of the oxide film [4].

2.3.   The Wagner Oxidation Theory

The Wagner oxidation theory played a major role on the understanding and prediction of high temperature oxidation of metals.   Under certain assumptions, it provides the theoretical foundation for the development of high temperature oxidation resistant metals and alloys [5].

During the formation of a dense oxide scale on an alloy, reactants and electrons are transported across the growing oxide scale. Complex reactions take place in the alloy/scale and scale/gas interfaces. If enough oxygen is available in the reaction atmosphere, the scale growth is often limited by the transport of ions or electrons through the scale. This is the case during most high temperature oxidation of metals and alloys [6]

The theoretical basis for the Wagner theory is based on the increasing scale thickness during oxidation. The increasing thickness results in an increasing transport length for the reactants and the driving force for the diffusing species will subsequently become smaller. This decreases the rate of scale formation as the scale thickness increases. The basic assumption in Wagner's theory is that the diffusion of reactants or the transport of electrons across the dense scale is rate determining for the overall oxidation process. This implies that the interfacial reactions are rapid, and thermodynamic equilibrium is assumed at the interfaces. Wagner's theory applies for the ideal case where the scale is dense and continuous and adheres well to the metal. The transport of ions through the scale is assumed to occur by lattice diffusion. Furthermore, ions and electrons are assumed to migrate independently of each other, and it is assumed that local equilibrium exists in the oxide.

During the formation of an oxide scale, the ions are transported through the scale by lattice diffusion, grain boundary diffusion or other short circuit diffusivity paths. Furthermore, several mechanistic factors play a role as the scale thickness increases. This includes loss of scale adhesion, creation of voids, porosity, etc. The implications of these additional features on the Wagner oxidation theory may be important.

2.4. Ionic Diffusion

During measurements of transport properties, it is often the tracer diffusion coefficient, which is measured. The tracer diffusion coefficient is related to the component diffusion coefficient via the Haven-ratio (H) [6]

$$D_{tr} = HD_K \qquad\qquad \text{Eq. 1}$$

The ionic transport in solids can often be described as a thermal activated hopping of defects to neighboring lattice sites. If the diffusion mechanism involves jumps to a nearby vacant site, it can be expected that the diffusion coefficient in proportional to the concentration of vacancies. A vacancy diffusion coefficient D_v can be defined as the ratio between the component diffusion coefficient and the mole fraction x_v of the available vacant sites

$$D_K = D_y x_y \qquad\qquad \text{Eq. 2}$$

Similar expressions can be written for other diffusion mechanisms. If more than one diffusion mechanism is involved, the general expression is

$$D_K = \sum_{Def} D_{Def} x_{Def} \qquad\qquad \text{Eq. 3}$$

The temperature dependence for the component diffusion coefficient is given by an Arrhenius-type expression [7].

$$D_K = A exp\left[\frac{\Delta S_f + \Delta S_m}{k}\right] exp\left[-\frac{\Delta H_f + \Delta H_m}{kT}\right] \qquad\qquad \text{Eq. 4}$$

Where A is a constant for the solid of interest [7]. The Gibbs energy of migration of defects is given by

$$\Delta G_m = \Delta H_m - T\Delta S_m \qquad \text{Eq. 5}$$

The Gibbs energy of formation of defects is given by

$$\Delta G_f = \Delta H_f - T\Delta S_f \qquad \text{Eq. 6}$$

The activation energy for diffusion is given by

$$E_A = \Delta H_f - \Delta H_m \qquad \text{Eq. 7}$$

And can be determined by plotting $\log(D_K)$ vs $1/T$ [8].

2.5. Parabolic Reaction Rate

Experimental kinetics results for the high-temperature scaling of metals and alloys are very often interpreted in terms of a parabolic rate law, with the apparent rate constant k_p calculated from a plot of the variation of the weight-gain squared per unit area, Δm^2 vs time t. But the high-temperature scaling kinetics of only a very limited number of pure metals and binary alloys might be described by the simplest form of the parabolic law:

$$\Delta m^2 = k_p t \qquad \text{Eq. 8}$$

For most metallic materials, particularly for complex alloys such as heat resisting alloys, the steady state parabolic kinetics are generally established only after a transient period of faster kinetics according to a different rate law or rate

constant. Depending on the specific oxidation behavior, the steady state parabolic law will be given by

$$\Delta m^2 - \Delta m_i^2 = k_p(t - t_i)...\text{(i) or } (\Delta m - \Delta m_i)^2 = k_p(t - t_i) ... (ii) \quad \text{Eq. 9}$$

For the first case, (i), the scale formed during the initial weight-gain Δm_i after the time t_i, does contribute to limiting the kinetics at steady state for $t > t_i$. The latter case (ii), which is the more commonly encountered, corresponds to the initial growth of a poorly protective oxide scale, e.g., NiO or FeO, whereby the later slower steady state parabolic kinetics may be related to the formation of a continuous and adherent protective oxide scale such as Cr_2O_3 or Al_2O_3. In this case, the initial scale with mass gain Δm_i after t_i does not contribute to steady state rate control [9].

2.6. Ellingham Diagrams

Ellingham diagram, also known as oxygen potential diagram, is a graphical presentation of oxidation/reduction reactions of various elements at all temperatures in oxygen, wet hydrogen, and carbon monoxide-carbon dioxide mixtures and has proved to be indispensable to understand reactive systems.

A general oxidation reaction can be written as

$$x\frac{b}{a}Me(s) + O_2(g) \leftrightarrow \frac{b}{a}Me_xO_{\frac{2a}{b}}(s)$$
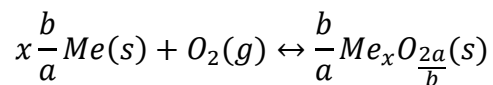
Where *Me* is the metal. The change in Gibbs free energy for the prior reaction can be written as

$$\Delta G = \Delta G^O + RT\ ln\frac{a(Me_xO_{2a/b})^{b/a}}{a(Me)^{xb/a}a(O_2)}$$

Eq. 10

If the activity of pure metals and oxides are one, and the oxygen partial pressure is used for the oxygen activity, i.e. *a(O₂)=pO₂,* at equilibrium Eq. 10 can be written as

$$\Delta G^O = -RTln\frac{1}{pO_2}$$

Eq. 11

ΔG^O is a function of temperature ($\Delta G^O = \Delta H^O - T\Delta S^O$), so plotting the standard Gibbs free energy for a reaction against the temperature will give straight lines provided that the standard reaction against the temperature will give straight lines provided that the standard reaction enthalpy and entropy does not change with temperature. These lines are plotted for a range of different oxides in Figure 1, such diagram is called Ellingham diagram.

At equilibrium for reaction from Eq. 11, the standard Gibbs free energy change can be associated with an oxygen pressure via Eq. 11

$$pO_2 = exp\frac{\Delta G^O}{RT}$$

Eq. 12

This pressure is the decomposition pressure for the oxides, i.e. the oxygen partial pressure corresponding to the metal-oxide equilibrium. These decomposition pressures can be shown on the Ellingham diagram. From Eq. 12,

it easily follows that $\Delta G^0 = RT \ln(pO_2)$. Hence, straight lines can be superimposed on the Ellingham diagram, where the slope defines the oxygen activity. The decomposition pressure for oxides at a given temperature can be found from these lines [10]. For example, the Cr/Cr_2O_3 decomposition pressure at 1000K is 10^{-31} bar as shown in Figure 1.
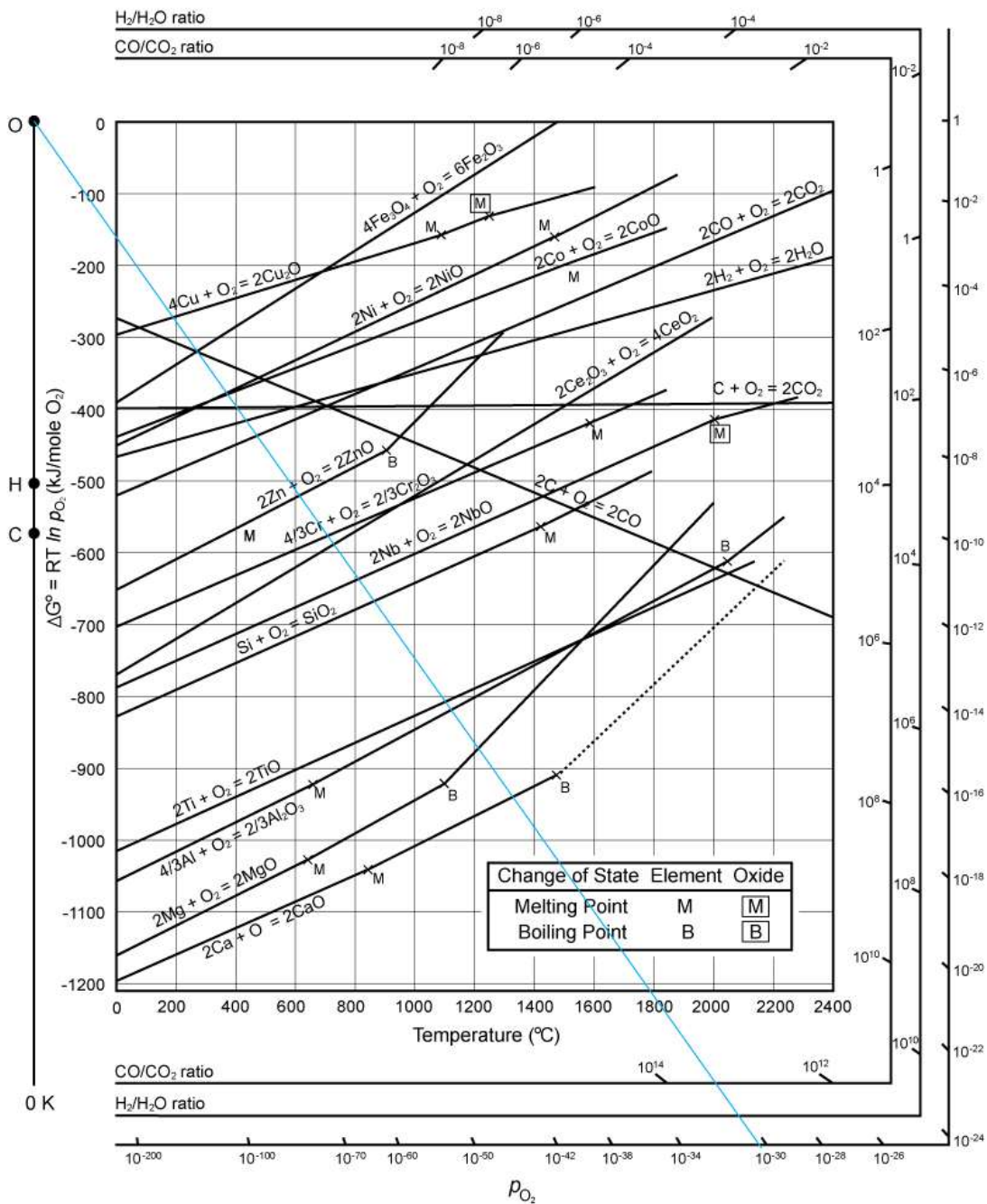
Figure 1. Decomposition pressures superimposed on the Ellingham diagram with calculation of decomposition pressure at 1000K for Cr/Cr2O3.

2.7. Zeta-Potential

The Zeta-Potential or electrokinetic is an important parameter of the electrical double layer and represents a characteristic of electrical properties of solid/liquid and liquid/gaseous interfaces. The potential difference between the external surface of that shell and the liquid as a whole is called Zeta-Potential, and it is used in colloid chemistry for observing the behavior of dispersive systems in liquids. Besides, the Zeta-Potential characterizes the electrical double layer on the solid/liquid interface, a fact very important in flotation and flocculation processes [11].

This double layer consists of charged surface and a neutralized surplus of opposite and equally-charged ions diffusely spreading through polar medium. The double layer is characterized by the ion arrangement and the magnitude of electrical potential in the vicinity of the charged particle surface. The existence of the electrical double layer is in close connection with the electrostatic interaction between the particles of suspension and, consequently, with the suspension stability. The electrical double layer consists of two parts, i.e. and inner part which includes adsorbed ions and an external or diffuse part in which the ions are arranged under the influence of electrical forces and thermal movements [12].

Three of the fundamental states of matter are solids, liquids and gases. If one of these states is finely dispersed in another then we have a colloidal system, i.e. aerosols, emulsions, colloidal suspensions and association colloids.

2.7.1. Colloidal Stability and DVLO Theory.

DVLO theory suggests that the stability of a colloidal system is determined by the sum of these Van der Waals attractive and electrical double layer repulsive forces that exist between particles as they approach each other due to the Brownian motion they are undergoing. This theory proposes that an energy barrier resulting from the repulsive force prevents two particles approaching one another and adhering together, Figure 2. But if the particles collide with sufficient energy to overcome that barrier, the attractive force will pull them into contact where they adhere strongly and irreversibly together.
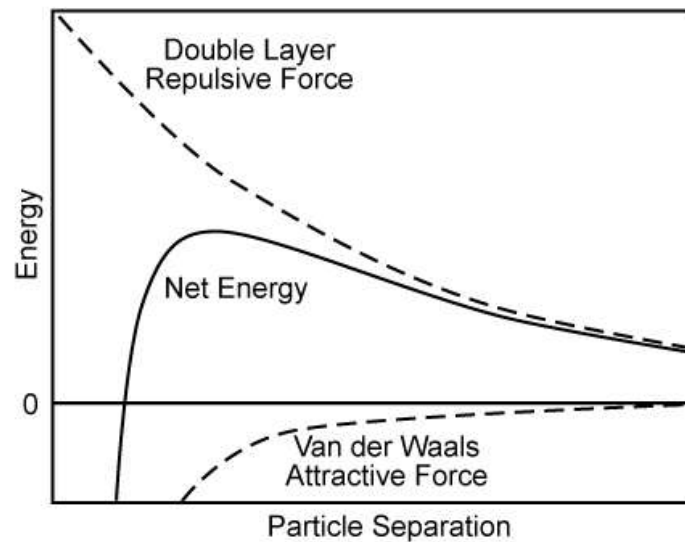
Figure 2. Schematic diagram of the variation of free energy with particle separation according to DVLO theory.

The magnitude of the zeta potential gives an indication of the potential stability of the colloidal system. If all the particles in suspension have a large negative or positive zeta potential then they will be no tendency for the particles

to come together. However, if the particles have low zeta potential values then there will be no force to prevent the particles coming together and flocculating.

The general dividing line between stable and unstable suspensions is generally taken at either +30 or -30 mV. Particles with zeta potentials more positive than +30mV or more negative than -30mV are normally considered stable. However, if the particles have a density different form the dispersant, they will eventually sediment forming a close packed bed [12].

2.7.2. Factors Affecting Zeta Potential

- *pH* is the most important factor that affects Zeta Potential, i.e. a particle in suspension with a negative zeta potential. If more alkali is added to this suspension then the particles tend to acquire more negative charge. If acid is added to this suspension then a point will be reached where the charge will be neutralized. The zero zeta potential is called the isoelectric point, where the colloidal system is least stable.

- *Conductivity*, the thickness of the double layer depends upon the concentration of ions in solution and can be calculated from the ionic strength of the medium. The higher the ionic strength, the more compressed the double layer becomes. The valency of the ions will also influence double layer thickness.

- *Concentration*, the effect of the concentration of a formulation component on the zeta potential can give information to assist in formulating a product to give maximum stability [13].

2.8. Coating

In oxidizing environments a metal may be protected from oxidation either by alloying or by coatings. In either case the objective is to form or obtain a layer on the metal surface which acts as a barrier separating the reacting gas and the underlying metal and as such inhibits the reaction between the reactants. In oxidizing environments at high temperatures, and if the oxygen pressures are not so low that oxygen adsorption becomes rate-limiting, a coating will in general owe its oxidation resistance to a protective oxide scale.

Table 1. The Conventional Application Techniques for Current Resistant Coatings [14].

Applications	Techniques
Gas turbine components	Spraying
Electrolytic cathode for copper refinement	Thermal Spraying
Water-cooled stator bars clips used in electrical generators	Chemical vapor deposition Physical vapor deposition
The semiconductor device and the liquid crystal device	Screen printing Dip-coating Thermal Spraying
The semiconductor processing equipment	Thermal Spraying Sputtering

	Immersion
	Chemical vapor deposition
	Physical vapor deposition
Alkaline-containing environment	Spraying
	Immersion
	Roll coating
High temperature erosion-corrosion environments	Thermal Spraying
	Spray and fuse
	Welding

2.9.   Substrate and Coating Materials

2.9.1. Austenitic Stainless Steel 316L

Types grade 316 and 316L are molybdenum-bearing austenitic stainless steel which are more resistant to pitting, crevice and general corrosion than the conventional chromium nickel austenitic stainless steel such as Type 304. These alloys also offer higher creep, stress-to-rupture and tensile strength at elevated temperature. Types 316 and 316L generally contain 2 to 3% molybdenum for improved corrosion resistance.

In addition to excellent corrosion resistance and strength properties, Types 316 and 316L alloys also provide the excellent fabricability and formability which are typical of the austenitic stainless steels.

Grade 316L, the low carbon version of 316 and is immune from sensitization (grain boundary carbide precipitation). Thus it is extensively used in heavy gauge welded components (over about 6mm).

The austenitic structure also gives these grades excellent toughness, even down to cryogenic temperatures.

Compared to chromium-nickel austenitic stainless steels, 316L stainless steel offers higher creep, stress to rupture and tensile strength at elevated temperatures.

These properties are specified for flat rolled product (plate, sheet and coil) in ASTM A240/A240M. Similar but not necessarily identical properties are specified for other products such as pipe and bar in their respective specifications.

Table 2. Composition ranges for 316L stainless steel

Grade		C	Mn	Si	P	S	Cr	Mo	Ni	N
316L	Min	-	-	-	-	-	16.00	2.00	10.00	-
	Max	0.03	2.00	0.75	0.045	0.03	18.00	3.00	14.00	0.10

A.   Properties and Characteristics

Corrosion Resistance

Excellent in a range of atmospheric environments and many corrosive media, generally more resistant than 304.   Subject to pitting and crevice corrosion in warm chloride environments, and to stress corrosion cracking above about 60°C.   Considered resistant to potable water with up to about 1000mg/L chlorides at ambient temperatures, reducing to about 500mg/L at 60°C.

Heat Resistance

Good oxidation resistance in intermittent service to 870°C and in continuous service to 925°C. Continuous use of 316 in the 425-860°C range is not recommended if subsequent aqueous corrosion resistance is important. Grade 316L is more resistant to carbide precipitation and can be used in the above temperature range. Grade 316H has higher strength at elevated temperatures and is sometimes used for structural and pressure-containing applications at temperatures above about 500°C.

Welding

Excellent weldability by all standard fusion and resistance methods, both with and without filler metals. Heavy welded sections in Grade 316 require post-weld annealing for maximum corrosion resistance. This is not required for 316L.

316L stainless steel is not generally weldable using oxyacetylene welding methods.

Machining

316L stainless steel tends to work harden if machined too quickly. For this reason low speeds and constant feed rates are recommended. 316L stainless steel is also easier to machine compared to 316 stainless steel due its lower carbon content.

Hot and Cold Working

316L stainless steel can be hot worked using most common hot working techniques. Optimal hot working temperatures should be in the range 1150-

1260°C, and certainly should not be less than 930°C. Post work annealing should be carried out to induce maximum corrosion resistance.

Most common cold working operations such as shearing, drawing and stamping can be performed on 316L stainless steel. Post work annealing should be carried out to remove internal stresses.

2.9.2. Cerium Oxide

Cerium is the most abundant of the rare earth elements, making up about 0.0046% of the Earth's crust by weight. It is found in a number of minerals including allanite (also known as orthite), monazite, bastnasite, rhabdophane, zircon and synchysite. Monazite and bastnasite are presently the two most important sources of cerium [15]

Cerium exhibits three oxidation states, +2, +3 and +4. The +2 state is rare and is observed in CeH_2, CeI_2 and CeS [16]. The most common compound of cerium is cerium (IV) oxide (CeO_2).

Cerium forms two oxides of ascertained composition, Ce_2O_3 and CeO_2. CeO_2 is the most stable oxide of cerium. This compound is also called ceria or ceric oxide. Cerium is the second member in the lanthanide series and ranked as the second most reactive element in the series. It is very electro-positive, and like other lanthanides, it has a Ce(III) oxidation state due to a low ionization potential for removal of the three most weakly-bound 4f electrons. However, the electronic structure for Ce(IV) is [Xe] 4f0, as compared with [Xe]4f1 for Ce (III),

is the most stable oxidation state in cerium due to the empty 4f0. From valence state theory, cerium is supposed to have two types of oxides, cerium dioxide (CeO_2) and cerium sesquioxide (Ce_2O_3). Since CeO_2 is the most stable oxide, when the cerium oxide is mentioned, it usually refers to the tetravalent oxide. Cerium dioxide can also be formed if cerium salt is calcined in oxygen rich environment [17].

A.   Physical Properties

Stoichiometric CeO_2 is pale yellow due to Ce (IV)-O charge transfer. However, since CeO_2 can be reduced in a reducing environment and Ce_2O_3 can be partially converted to CeO_2, it is usual that cerium oxide is an oxygen-deficient, non-stoichiometric oxide (CeO_{2-x} with $0<x<=0.5$). The nonstoichiometric cerium oxides appear with darker colors [18, 19]. Cerium oxide is highly stable, with a melting point of $2600°C$,.

B.   Crystal Structure.

Cerium sesquioxide (Ce_2O_3) has two structural forms, hexagonal and cubic. Cerium oxide (CeO_2) has a fluorite (CaF_2) structure (fcc) with space group Fm3m. Figure 3, illustrates the structure of the stoichiometric CeO_2 with the oxygens (represented by the gray internal solid spheres) four coordinated and the cerium (represented by the external solid spheres) eight coordinated. The cerium is at the center of tetrahedron and the tetrahedral corners are occupied by oxygens [20].

Usually, cerium oxide exists as a non-stoichiometric oxide that is a mixture of Ce(III) oxide and Ce(IV) oxide, while still retaining the fluorite cubic structure.
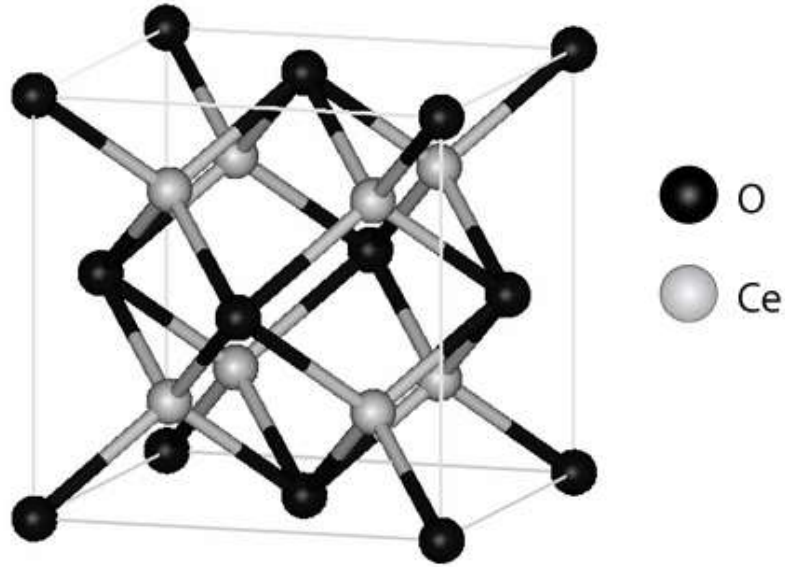
Figure 3. FCC structure for CeO_2

C.   Hydrophobicity of Rare Earth Oxides (REOs)

The origin of the hydrophobicity of the REOs can be attributed to their electronic structure. While most ceramics and metals are hydrophilic, due to coordinative unsaturation, which allows water to form bonds with available valence orbitals, the 4f orbitals of rare-earth atoms are completely shielded by the electrons in the filled 5s and 5p orbitals. They are thus not available to hydrogen bond with water molecules [21]

D.   Colloidal Dispersion of Cerium Oxide

For this research a commercial solution of Cerium Oxide was purchased from Sigma Aldrich. The solution of Cerium (IV) Oxide is a 20 wt. % colloidal dispersion in 2.5% acetic acid, with a 10 to 20 nanometers average particle size.

E.   Effects of Acetic Acid on Cerium solutions

It has been found from the potentiodymamic curves that by increasing the acetic acid/$CeCl_3$ molar ratio, high uniform films with well-developed grains were obtained and grain sizes of the films decreased. By increasing the acetic acid ratio from X=0 to X=1 and X=2, the amount of corrosion rate decreased and the best corrosion resistance was obtained when the molar ratio of acetic acid with respect to cerium chloride was about 2. The mean average size of the crystalline grain is observed to diminish by using acetic acid [22].
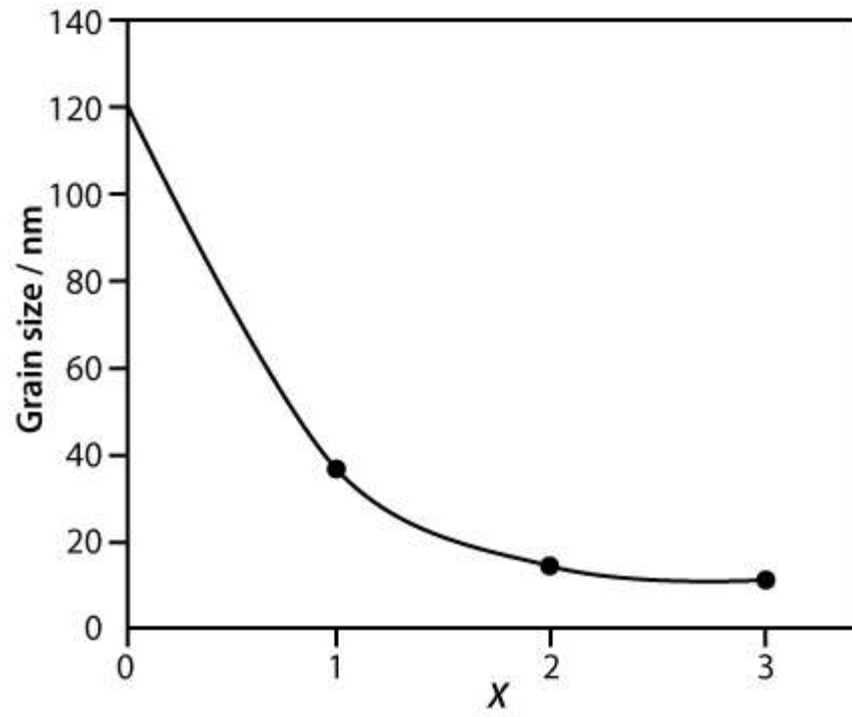
Figure 4. Curve of the grain size of the nano cerium oxide film with different acetic acid/CeCl$_3$ molar ratios (X=0, 1, 2, 3) on samples.

3. EXPERIMENTAL PROCEDURES

3.1. Substrate Surface Preparation

The preparation of a metal surface, necessary to achieve good bonding between substrate and coating, must be sufficient to remove several types of contaminant, ranging from metal corrosion products (oxide, sulphide, scales, etc.) to soil contamination (oil, grease, dirt, etc). Usually several stages of preparation are necessary and will be selected as appropriate for any particular substrate treatment. [23]

The samples of austenitic stainless steel 316L were cut into 30 mm x 20 mm with a thickness of 0.72 mm with a punch hole of 2 mm in diameter at the center near to the edge of the narrow area.

The substrates were mechanically polished using a 1200 grit SiC paper, rinsed with DI water. Chemically cleaned immersed in 2-propanol, 99.5%, HPLC grade; and placed in the ultrasonic cleaner for 5 minutes and subsequently air-dried.

After these treatments the substrates were isothermally pre-oxidize in air at 700°C during 2 min and cooled in air to room temperature. Pre-oxidation improves surface wetting and helps form well-adherent coating. [10]

The weight of each sample before and after applying the coating layers was measured using a microbalance Sartorius, Model LA 230S, with an accuracy of 0.0001 g.
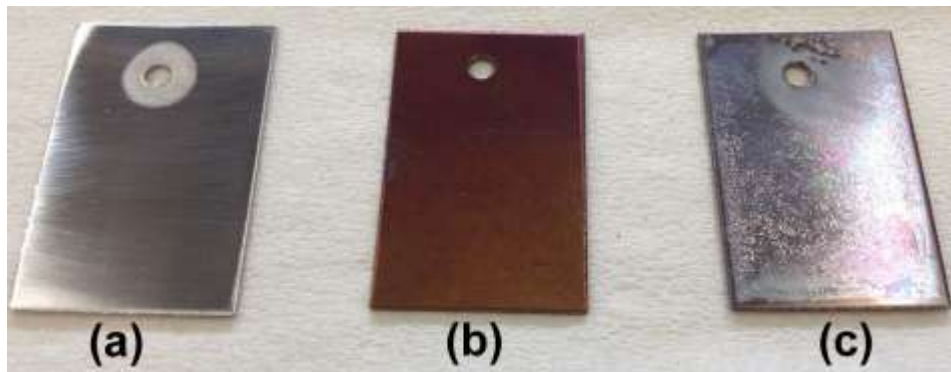
Figure 5. Austenitic Stainless Steel 316L samples, dimensions: 30 mm x 20 mm x 0.72mm. (a) Bare sample. (b) Pre-oxidized sample. (c) Coated sample.

3.2.   Coating Deposition

The deposition of the coating has been applied using a spraying coating method. An Iwata CM-SB airbrush was used with a mini oil-less airbrush compressor. The Iwata CM-SB airbrush has a paint reservoir, side-feed cup of 1/8 oz. (3.8 ml); with a nozzle of 0.18 mm matched head system; with a dual-action trigger; and with a spray pattern, micro-line to ¾ in. (20 mm) round. The mini oil less airbrush compressor, with a tank capacity of 3 liters, 7 bars (100 psi). The air delivery is 23 liter per minute with 1/5 of horse power.

The ideal method application of the coating was defined through trial. Based on a consistent thickness layer with a homogeneous distribution; using

different distance applications and pressure settings. Two layers of coating were deposited to each individual substrate sample. Each layer was applied perpendicularly with a distance of 3 inches between the tip of the airbrush and the substrate sample; with an air pressure of 45 psi delivered from the mini oil less airbrush compressor and a setting of 1.5 in the airbrush. After the application of each layer the samples were dried at 100°C for 3 minutes using a Fisher Scientific, Isotemp Oven 516G, with a temperature range: ambient to 210°C (+-5°C).

3.3. Humidity Calculation as a Function of Water Temperature

Water vapor is a key constituent of the atmosphere and plays a significant role in thermodynamic processes that affect the evolution of the atmospheric state through time. Typically water vapor is represented by the variable relative humidity, the amount of water vapor in the mixture of water vapor and dry air. The relative humidity, which is the maximum amount of specific humidity (Figure 6) that the air can contain at a given temperature and pressure, has been based on the calculation from Table 3.

In this work, the term "relative humidity" refers to the volume percent of water in the atmosphere. A value of 10% RH means that the test gas contains 10% by volume water vapor with the balance being air.

Table 3. Values of Specific Humidity as a function of water temperature and oxygen air flow pressure.

Specific Humidity	T (°C)	Pws (Pa)	Pw (torr)	G/kg (water to air)
0.85%	5.0	860.856	6.457	0.00533
2.28%	20.0	2309.651	17.324	0.01451
5.49%	35.0	5560.938	41.710	0.03612
10.00%	46.3	10135.441	76.022	0.06913
19.47%	60.0	19724.264	147.944	0.15034
30.46%	70.0	30866.165	231.515	0.27247
56.53%	85.0	57281.461	429.646	0.80893
68.58%	90.0	69485.077	521.181	1.35736
82.69%	95.0	83783.705	628.429	2.97081
99.13%	100.0	100445.856	753.406	71.06382
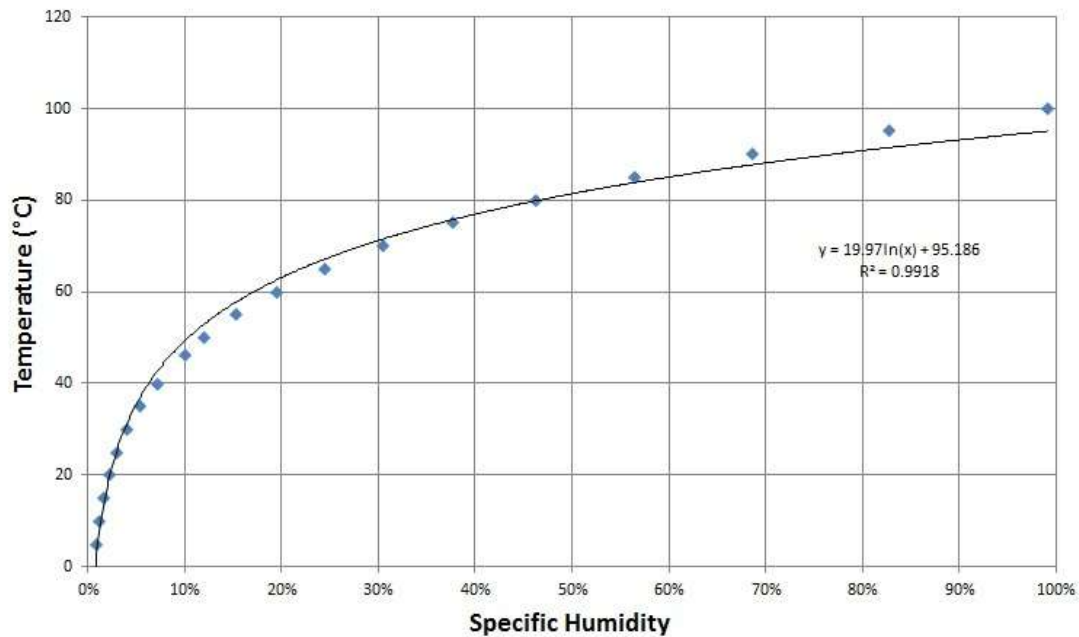
Figure 6. Specific Humidity vs. Temperature.

3.4.   Characterization Techniques

3.4.1. Light Scattering Technique

For the Light Scattering technique is used a Brookhaven Instrument ZetaPALS-Zeta Potential Analyzer. The principle of dynamic light scattering is that fine particles and molecules that are in constant random thermal motion, called Brownian motion, diffuse at a speed related to their size, smaller particles diffusing faster than larger particles. To measure the diffusion speed, the speckle pattern produced by illuminating the particles with a laser is observed. The scattering intensity at a specific angle will fluctuate with time, and this is detected using a sensitive photodiode detector. The intensity changes are analyzed with a digital autocorrelator which generates a correlation function. This curve can be analyzed to give the size and the size distribution.

3.4.2. Atomic Force Microscope (AFM)

Atomic Force Microscope can achieve atomic resolution by using a sharp cantilever tip. Images obtained by AFM can distinguish two closely spaced atoms. The image is created by quantifying the forces between the probe (cantilever tip) and the sample surface. AFM is a method to visualize the shape of a surface in three-dimensional (3D) detail down to the nanometer scale. AFM can image all materials –hard or soft, synthetic or natural (including biological structures such as cells and biomolecules)- irrespective of opaqueness or conductivity. The sample is usually imaged in air, but can be in liquid

environments and in some cases under vacuum. The surface morphology is not perceived in the usual way, that is, by line-of-sight, reflections, or shadows. Rather, at each point or pixel within a 2D array over the surface, a measurement of surface height is made using a sharp solid force probe. One could thus say that AFM is "blind microscopy"; it essentially uses touch to image a surface, unlike light or electron microscopes. Typically, one chooses to display the height measurements as colors or tints, some variant of dark-is-low/bright-is-high, with a gradient of color or grayscale in between. [24]

3.4.3. Thermogavimetric Analsys (TGA)

Thermogravimetric analysis (TGA) or thermogravimetry, is one of the thermal analysis methods that consist in recording continuously the change of mass of a sample in a controlled atmosphere as a function of temperature and time; as a change or increment of temperature affecting the sample.

Parts of the custom built TGA instrument consist of: (A) an analytical microbalance with 7 digits of sensitivity(1 microgram resolution), (B) a high temperature tube furnace type Thermolyne 54500, (C) heating control unit for the furnace, (D) a purge gas system for providing an inert or reactive atmosphere, (E) purge gas system for protecting the microbalance function, (F) heating tapes and control units for relative humidity control, (G) a computer for instrument control, data acquisition and display. As shown in the Figure 7.
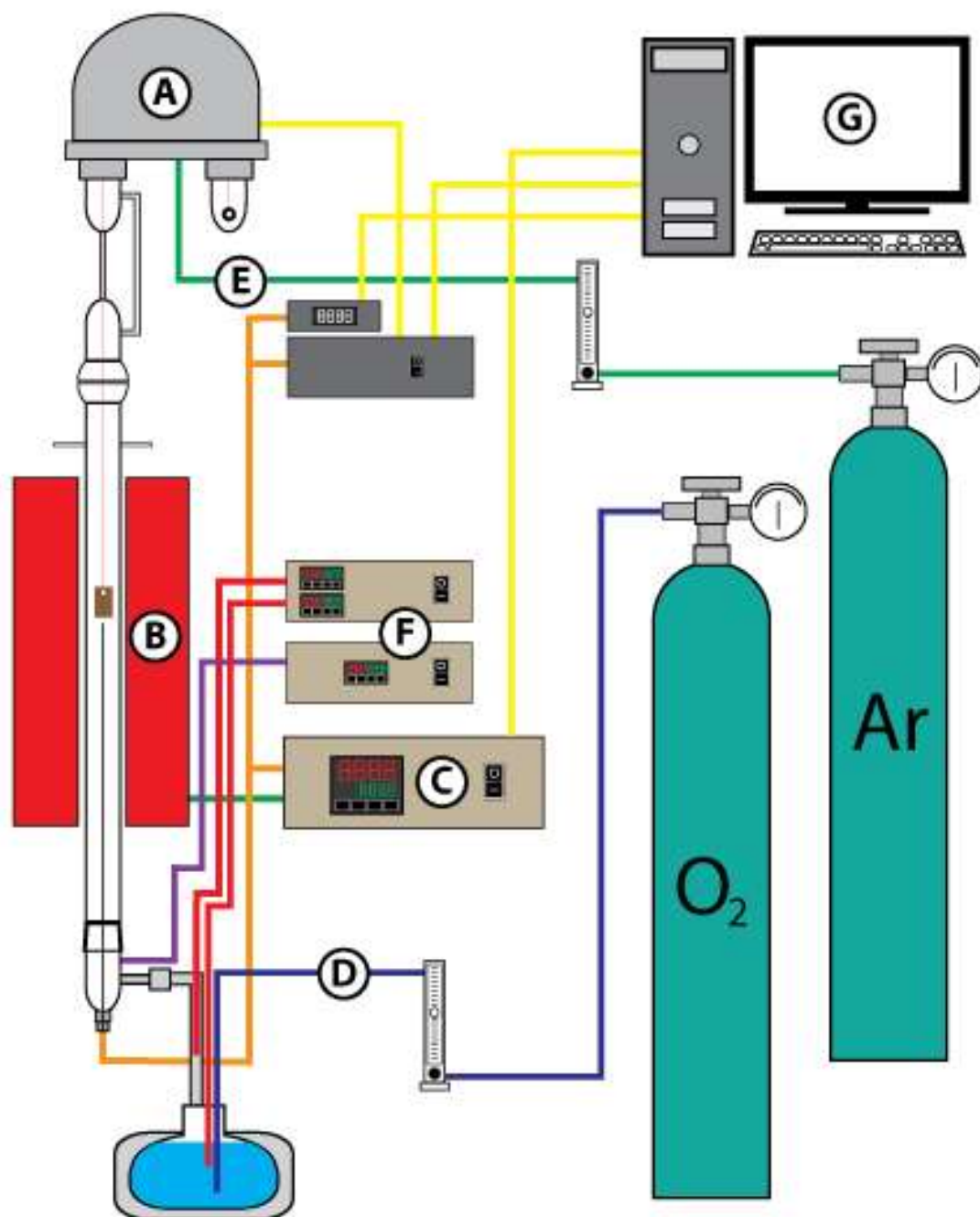
Figure 7. Schematic of the custom build Thermogravimetric Analysis Equipment.

3.4.4. Scanning Electron Microscopy (SEM) and Energy Dispersive Spectroscopy (EDS)

The Scanning Electron Microscope (SEM) has the advantage over optical microscopy of greater resolutions and magnifications. As a surface sensitive technique, the SEM can be used in applications where topographic information is important, such as for coating textures or for powder characterization, where the imaging capability provides information on uniformity, size and shape. EDX allows quick, semi-quantitative sample characterization and can be used to identify surface contamination and impurities located by the SEM examination. The SEM used in this work was a TopCon SM-300 with a Si(Li) EDS detector. Operating voltages ranged from 10 to 20 kV.

3.4.5. X-Ray Diffractomety (XRD)

X-ray diffraction is analysis technique typically used for phase identification and to establish the crystallinity of a given material.

When an x-ray beam penetrates a crystal structure, it will interact with the arranged atoms in the crystal. A portion of this incident beam will be reflected in the form of a diffracted beam. Constructive interference of these diffracted rays can only exist in certain diffraction angles and can be described by Bragg's law as follows:

$$n\lambda = 2d_{hkl}\sin\Theta \qquad\qquad\qquad \text{Eq. 13}$$

Where λ is the wavelength of the x-rays, n is an integer number and the order of diffraction, *d* is the interplanar spacing in the crystal, *hkl* are the Miller indexes of the plane, and Θ is Bragg's angle.

The XRD instrument used in this work was a Scintag 2000 operated with a copper X-ray source at 40 kV.

4. EXPERIMENTAL RESULTS

4.1. Effective Diameter Size Characterization using Light Scattering Technique

The measurement of the nanoparticles of the commercial solution from Sigma Aldrich, a 20 wt. % colloidal dispersion of Cerium Oxide (CeO_2) in 2.5% of acetic acid; was characterized using a Light Scattering technique using a Brookhaven Instrument ZetaPALS-Zeta Potential Analyzer. The capability of this instrument only measures the size of the agglomeration (effective diameter size) of the nanoparticles without detecting a single particle. The average effective diameter size is 19.2 nanometers, as shown in the Figure 8, within the range of values reported. The 20 wt. % colloidal dispersion of Cerium Oxide (CeO_2) in 2.5% of acetic acid, reported in the product specification a range of 10 to 20 nm average of particle size,
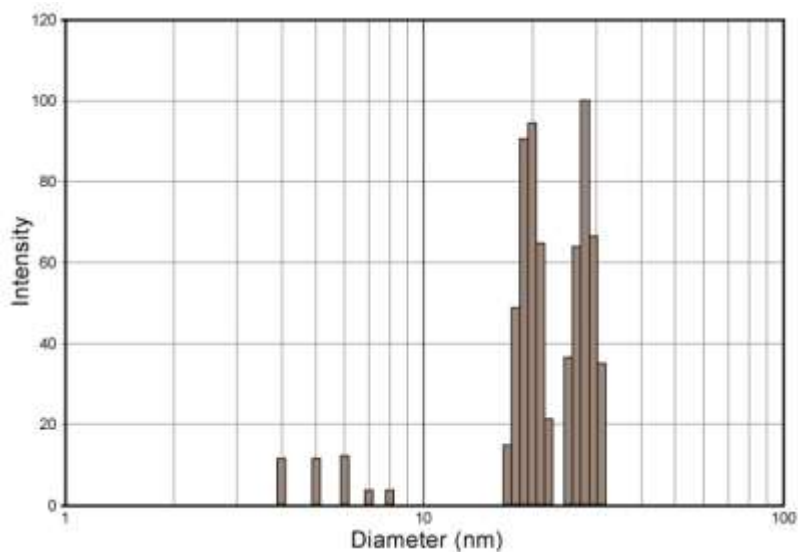

Figure 8. Multimodal size distribution of the effective diameter size of cerium oxide nanoparticles.

4.2.   Thickness and Surface Analysis-AFM

The thickness and surface of the coating was characterized using an Agilent Technologies 5420, Atomic Force Microscope; characterizing a surface of 1 micron square area.

A coating of 20 wt. % colloidal dispersion of Cerium Oxide (CeO_2) in 2.5% of acetic acid was applied using the same spraying method used for the all the samples on a silica (111) wafer substrate of 1 x 1 cm, and was annealed at 100C during 3 minutes. Figure 9, shows the AFM micrograph and it shows the topography of the coating over the substrate. The morphology of the surface and size of the coating of nanoparticles of cerium oxide is approximately 180 nm to 1.5 μm, shown in Figure 10. The thickness of the coating can be as thin as 180 nm using the spraying coating method. Uniform thin layers is desired for the deposition of cerium oxide. Increasing film thicknesses increase porosity and cracking in the surface.
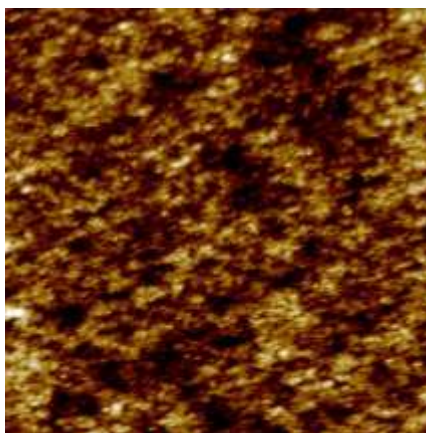

Figure 9. AFM micrograph, topography of the cerium oxide coating.
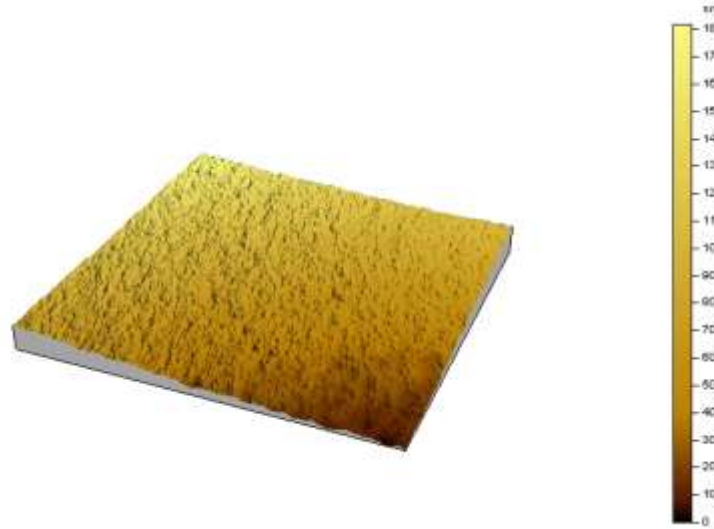
Figure 10. AFM micrograph, thickness characterization of the cerium oxide coating over a silicon wafer.

4.3.   Isothermal Oxidation through Thermogravimetric Analysis (TGA)

The oxidation tests were performed using a custom built Thermogravimetic Analysis instrument (Figure 12) capable of controlling temperature, relative humidity conditions and weight change. The tempered glass chamber can host samples as big as 25 x 50 mm and 5 mm thickness. A stream of water-saturated flow air is combined with a stream of dry air to produce desired relative humidity levels. The humidity conditions flows are adjusted using customized heat controlled units, pumping the water-air flow into the TGA chamber at a constant pressure using pure O_2. Using two additional heat control points at the connection area and the inlet at the base of the chamber to avoid condensation and keeping the water-air flow at constant rate.
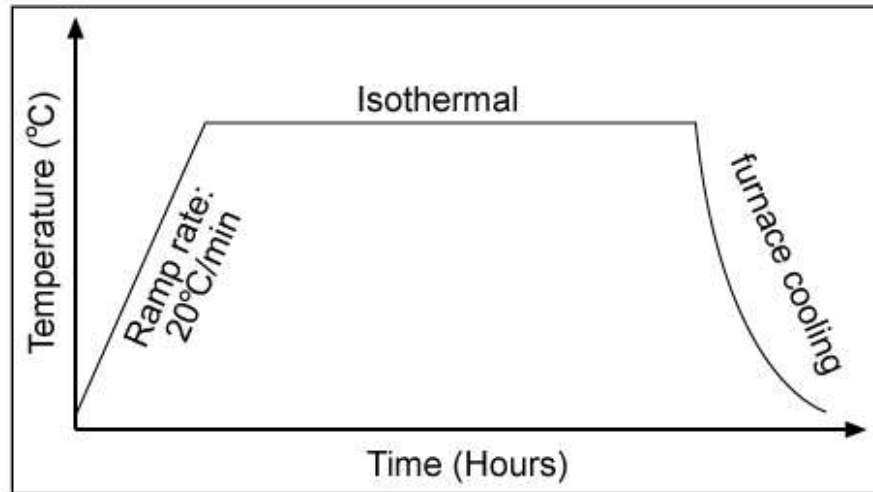
Figure 11. Heating cycle for isothermal oxidation.

The heating cycle starts at room temperature and reach the specific isothermal temperature of 750°C, 800°C or 850°C; at a ramp rate of 20°C/min, after a period of time of 16 hours, the furnace power supply it is shut down and is allowed to cool down to room temperature, as shown in Figure 11.

Figure 12. Custom built Thermogravimetric Analysis Equipment

4.4.   Oxidation Reaction Rate and Experimental Kinetics

Experimental kinetics results for the high temperature oxidation test of the cerium oxide coatings in the austenitic stainless steel 316L substrates are interpreted in terms of a parabolic rate law, with the apparent rate constant *kp* (slope), calculated from a plot (or a least-squares refinement) of the variation of the weight-gain squared per unit area, Δm^2 vs time t (g^2/cm^4 vs hr).

For most metallic materials, particularly for complex alloys such as heat resisting alloys, the steady state parabolic kinetics are generally established only after a transient period of faster kinetics according to a different rate law or rate constant. The plot of the kinetics data $\Delta mass^2/Area^4$ vs. t plot for the determination of a parabolic rate constant for steady state parabolic behavior following some faster transient growth of an initial scale, is graphically display.

Table 4. Test matrix conditions to study the impact of relative humidity and temperature of nano cerium oxide coating on 316L austenitic stainless steel.

Cerium oxide coating on 316L austenitic stainless steel			
Temperature	% Relative Humidity		
750C	0%	10%	20%
800C	0%	10%	20%
850C	0%	10%	20%

The following graphs show the weight gain during the oxidation time, the samples were oxidized at 750°C, 800°C and 850°C at 0%, 10% and 20% of relative humidity, respectively, as shown in Table 4.

Figure 13. Time vs. Mass, isothermal at 750∘C and 0% of Relative Humidity during 16 hours.

Figure 14. Time vs. Mass, isothermal at 800∘C and 0% of Relative Humidity during 16 hours.

Figure 15. Time vs. Mass, isothermal at 850◦C and 0% of Relative Humidity during 16 hours.

Figure 16. Time vs. Mass^2/Area^4, kp calculation from isothermal at 750◦C, 800◦C and 850◦C, with 0% of relative humidity.

Figure 17. Time vs Mass, isothermal at 750◦C and 10% of Relative Humidity during 16 hours.

Figure 18. Time vs. Mass, isothermal at 800◦C and 10% of Relative Humidity during 16 hours.
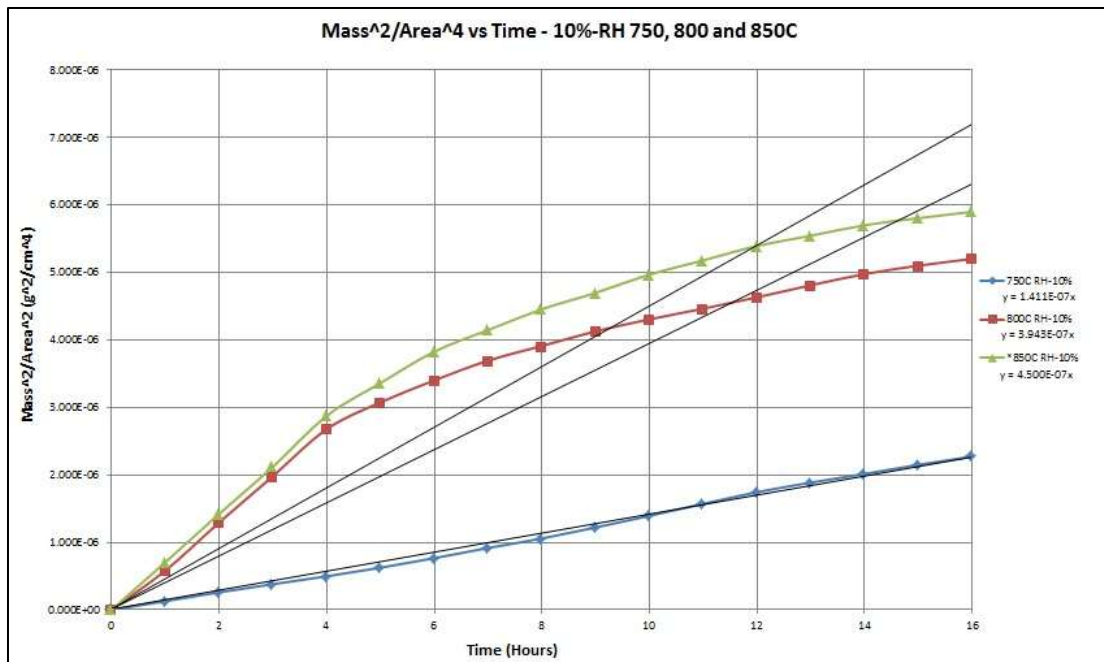
Figure 19. Time vs. Mass²/Area², kp calculation from isothermal at 750°C, 800°C and 850°C, with 10% of relative humidity.
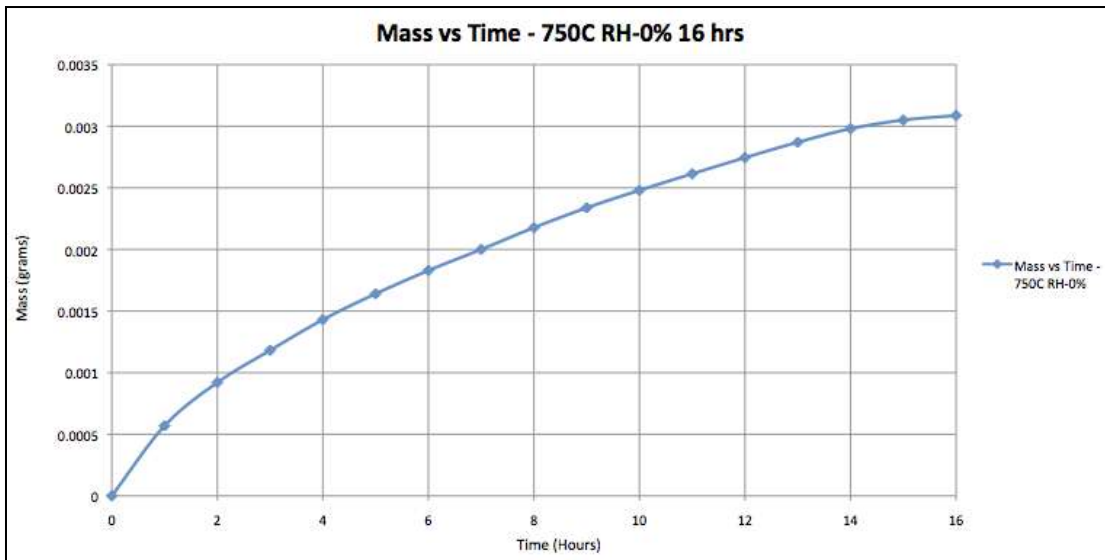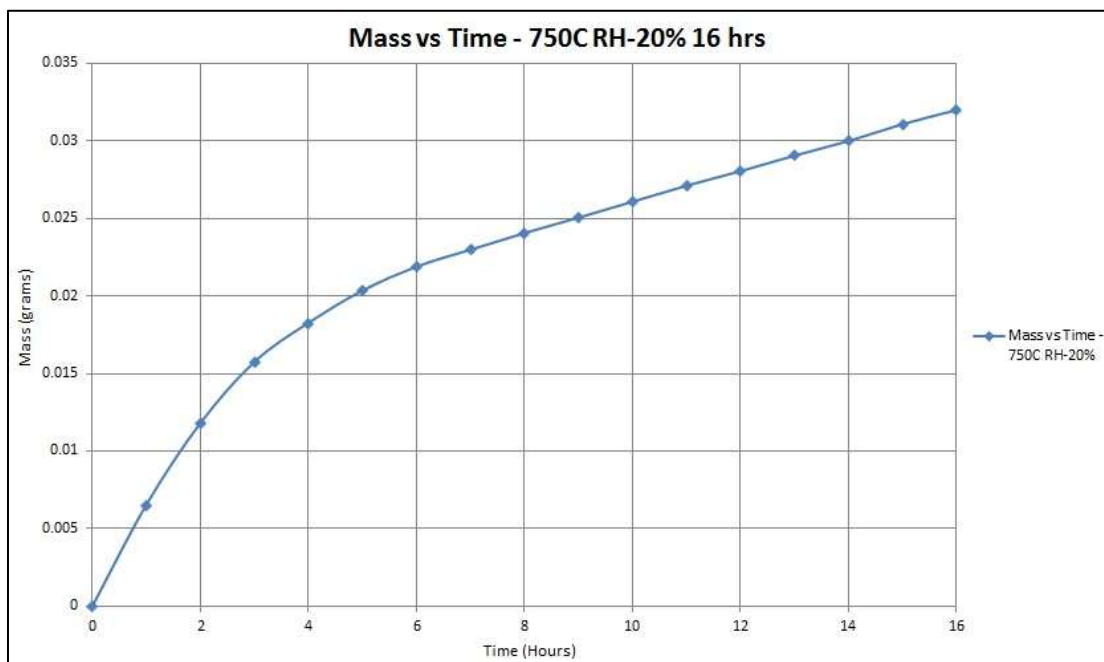

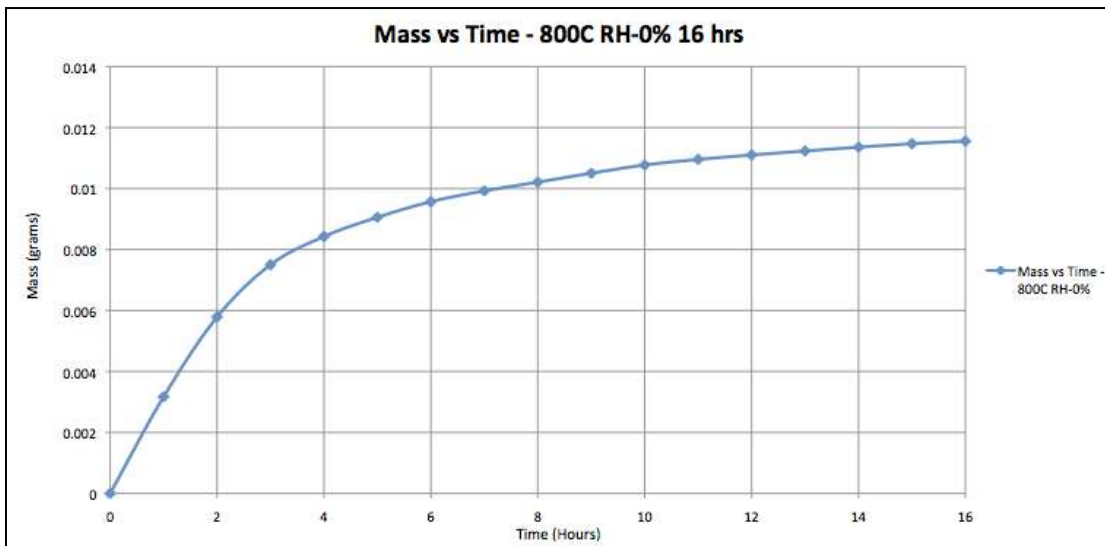Figure 20. Time vs. Mass, isothermal at 750°C and 20% of Relative Humidity during 16 hours.

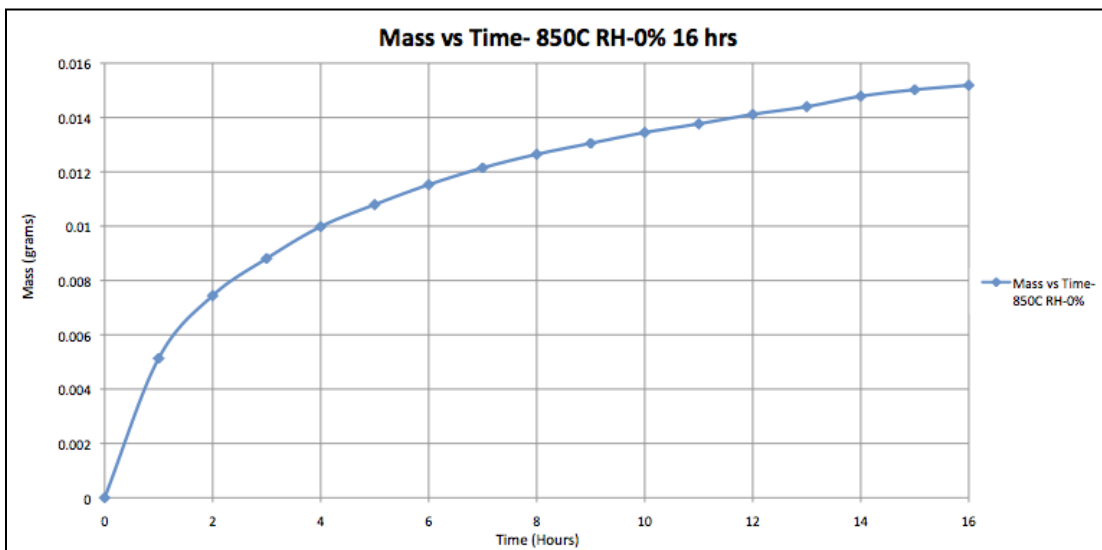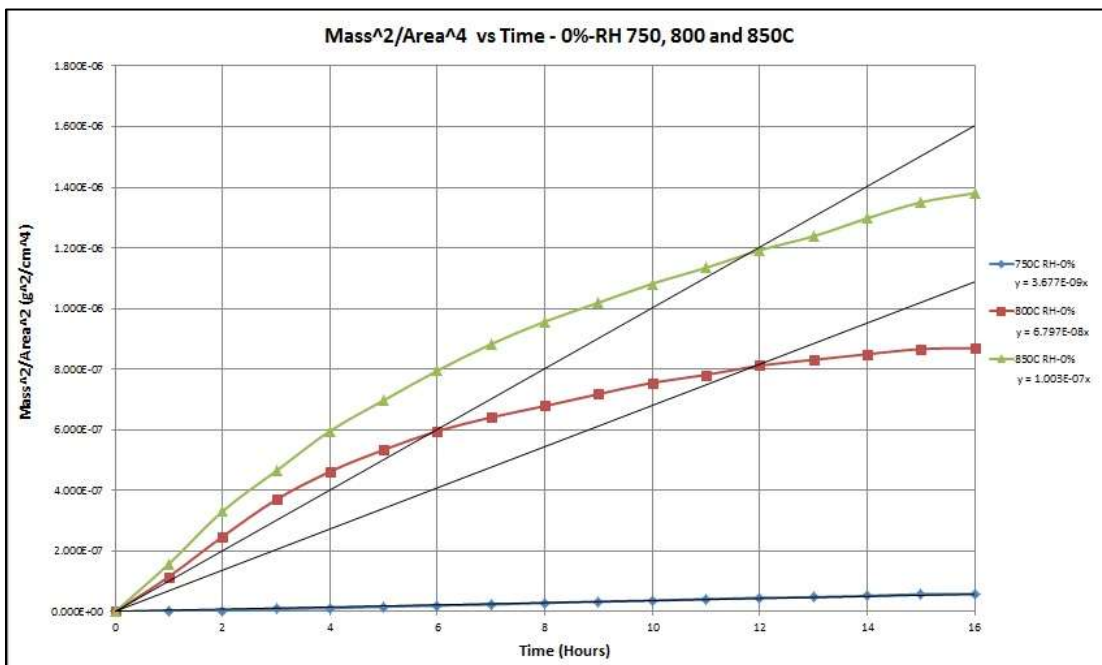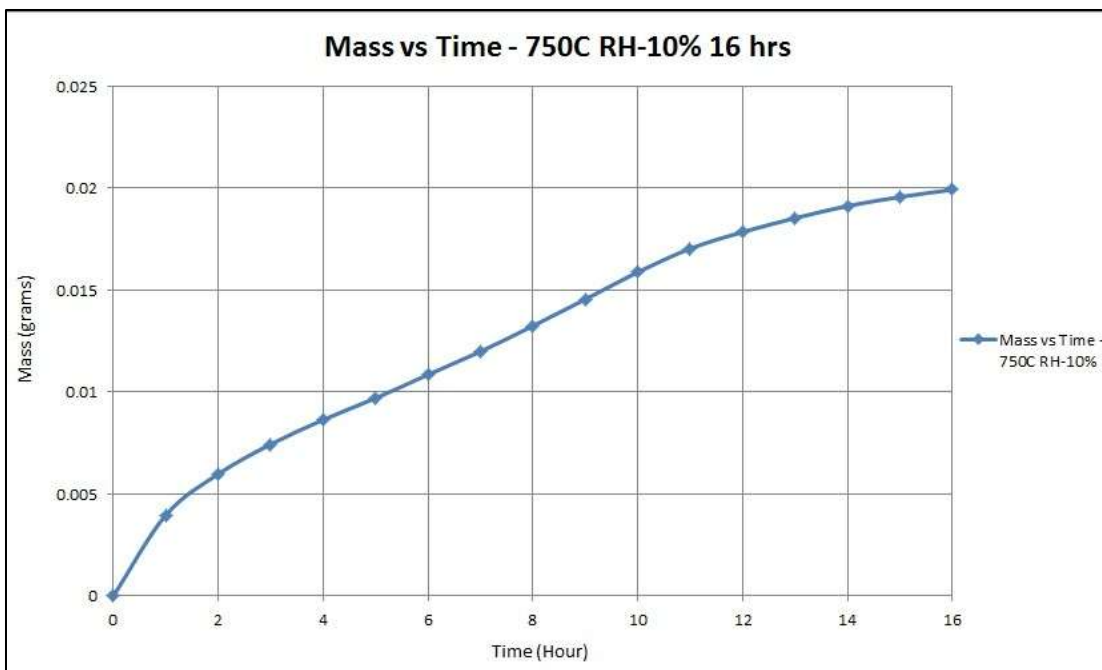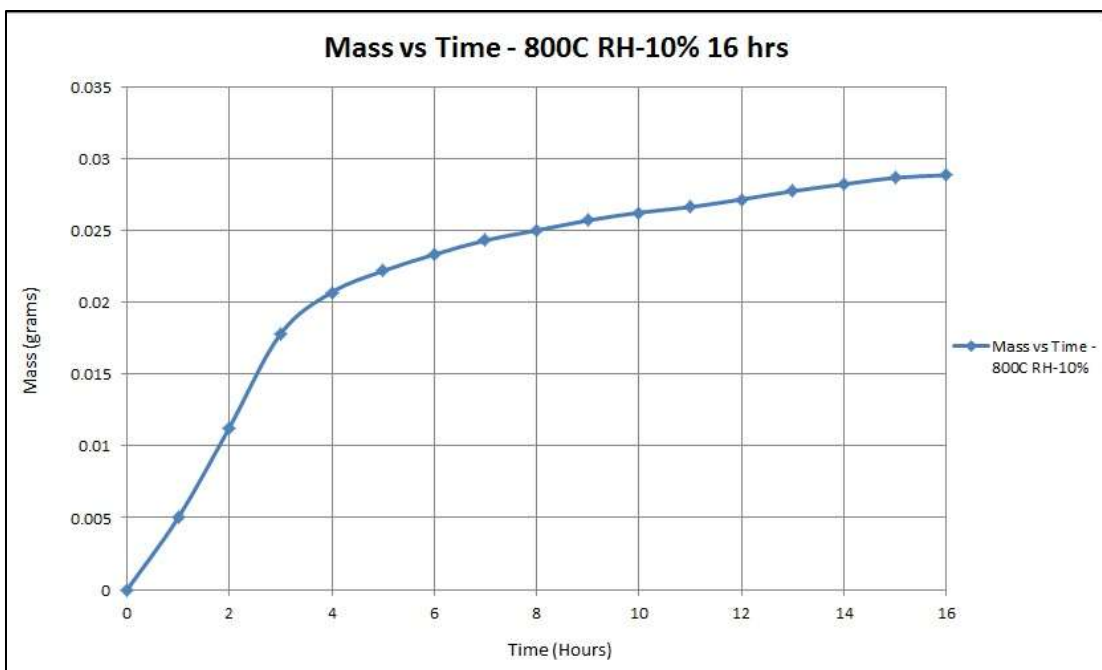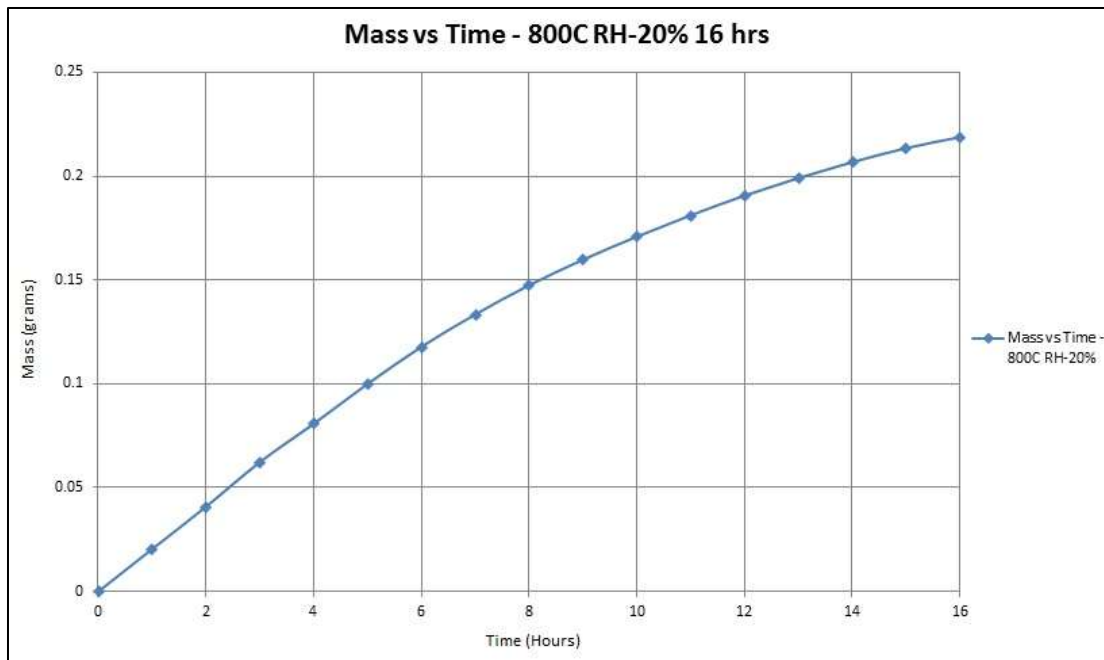Figure 21. Time vs Mass, isothermal at 800ºC, 20% of Relative Humidity during
16 hours.
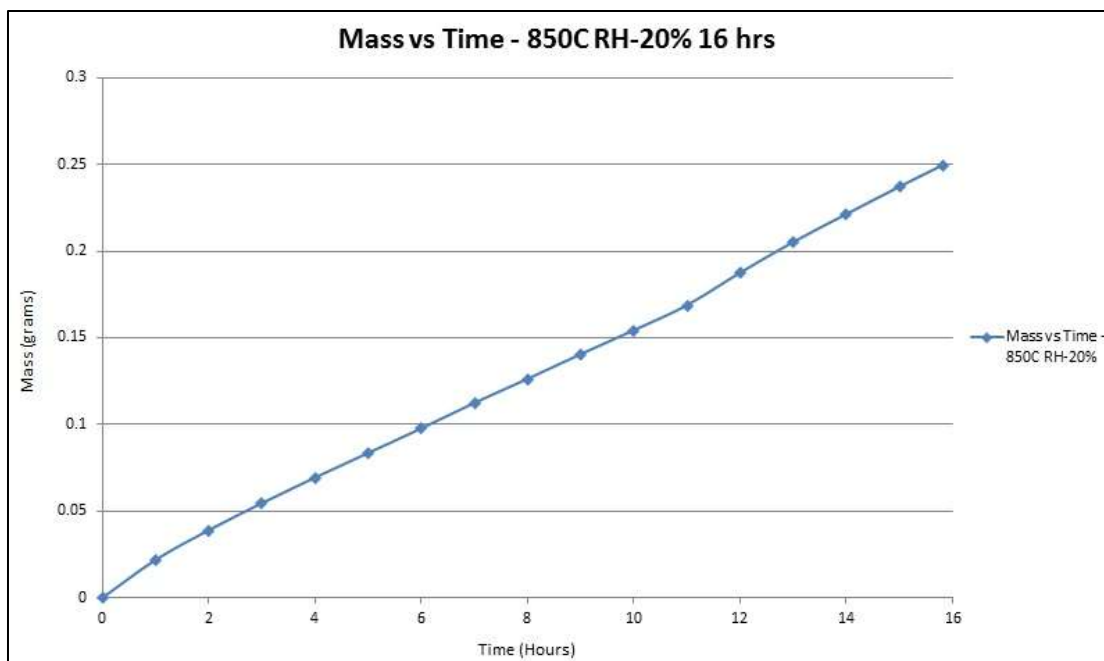
Figure 22. Time vs Mass, isothermal at 850ºC and 20% of Relative Humidity
during 16 hours.
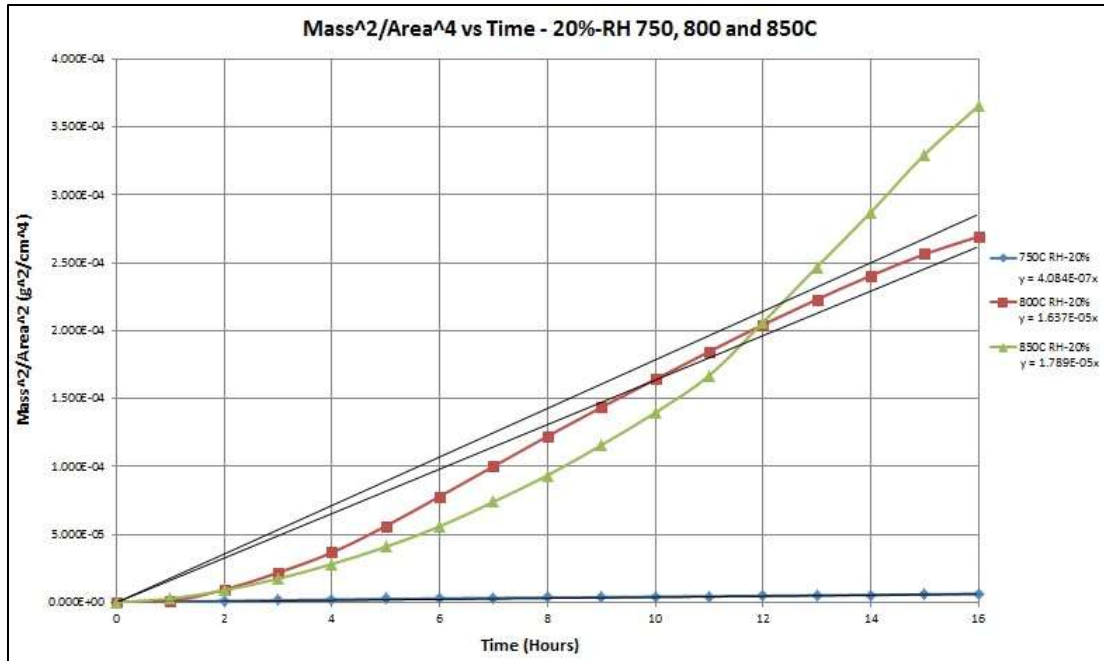
Figure 23. Time vs Mass^2/Area^4, kp calculation from isothermal at 750℃, 800℃ and 850℃, with 20% of relative humidity.

Table 5. Matrix of parabolic rate constants, kp, from isothermal oxidation exposure at 750℃, 800℃ and 850℃, with relative humidity levels: 0%, 10% and 20%

		Kp (g^2/cm^4)/h		
Temp (K)	Temp (^{o}C)	0% RH	10% RH	20% RH
1023	750	3.677E-09	1.411E-07	4.084E-07
1073	800	6.797E-08	3.943E-07	1.637E-05
1123	850	1.003E-07	*4.500E-08	1.789E-05

*Estimated value.

Table 6. Matrix of parabolic rate constants, and conversion to temperature 1000/K and Ln kp, with relative humidity levels: 0%, 10% and 20%.

		Ln kp		
Temp (1000/K)	Temp (C)	0% RH	10% RH	20% RH
0.0009775	750	-1.942E+01	-1.577E+01	-1.471E+01
0.0009320	800	-1.650E+01	-1.475E+01	-1.102E+01
0.0008905	850	-1.612E+01	*-1.461E+01	-1.093E+01

*Estimated value.
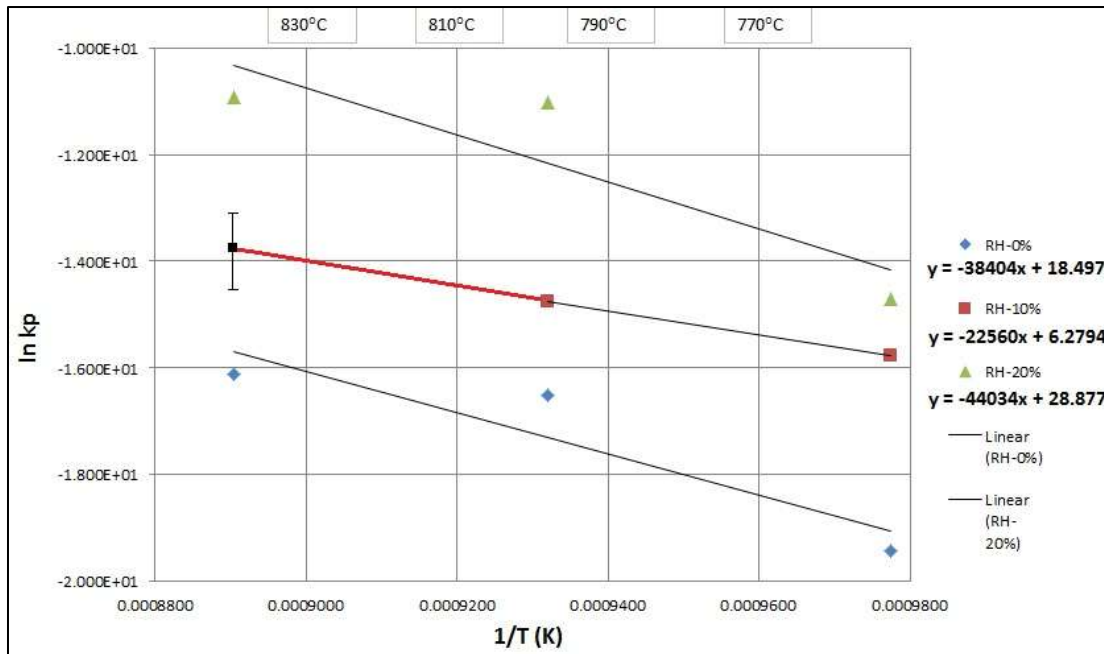
Figure 24. Partial pressures of CeO$_2$ coating at 0%, 10% and 20% of relative humidity.

The activation energy was experimentally calculated from the kp oxide formation in the Figure 24.

Table 7. Oxide formation activation energies, E_a, at 0%, 10% and 20% of relative humidity of Cerium Oxide coatings

Relative Humidity	E$_a$, Activation Energy (KJ/mol)
0%	319.29
10%	*343.00
20%	366.10

*Estimated value

4.5.   SEM – Analysis and Characterization

The topography of the bare substrate shows the nucleation of small oxide grains, the grains grow and agglomerate in a homogenous oxide film in the surface area as the oxidation reaction occurs, Figure 25.

The EDX analysis of the oxidized substrate shows the increasing content of chromium peaks as well as the presence of oxygen and decreasing content of iron, Figure 26; suggesting the formation of Cr_2O_3 as the main oxidation process in the 316L substrate at high temperatures.
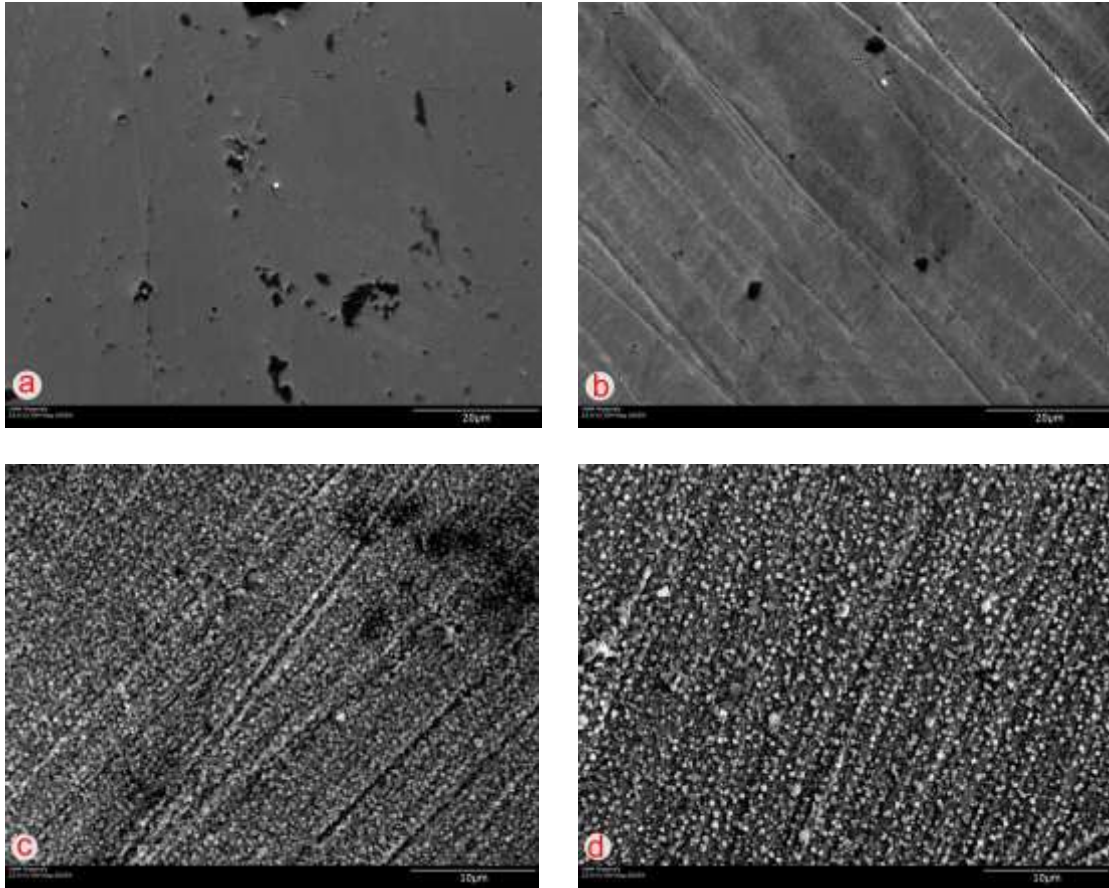
Figure 25. SEM micrographs of substrates with no coating [a] Bare substrate (316L) no oxidation, 1000x [b] Pre-oxidized substrate (2 min. at 700ºC dry air), 1000x [c] Bare substrate at 800ºC and 0% of Relative Humidity, 2000x [d] Bare substrate at 800ºC and 10% of Relative Humidity 2000x.
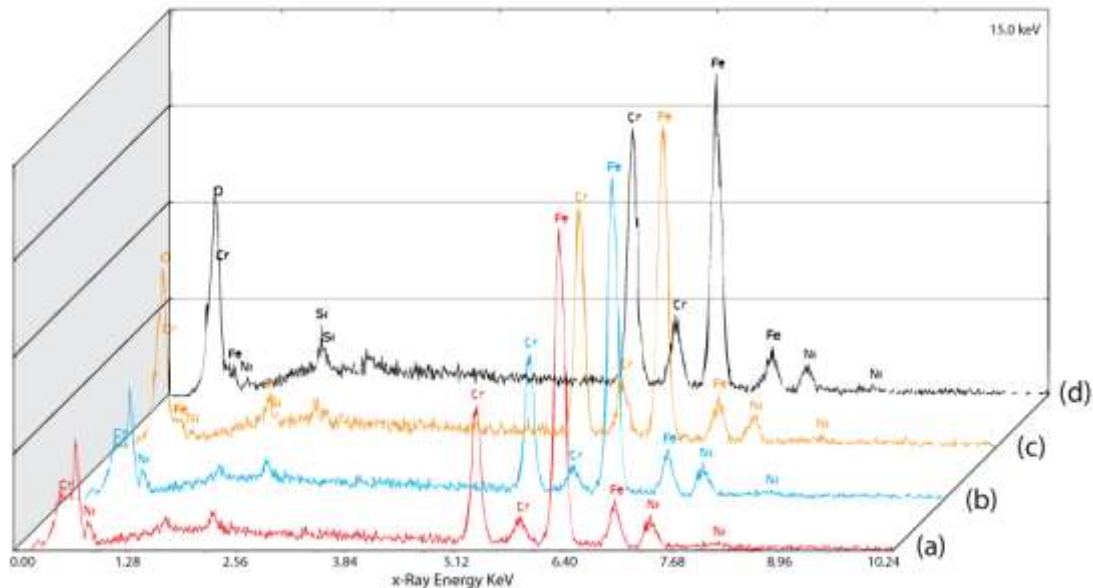
Figure 26. EDS spectrum analysis of bare substrate samples with no coating applied [a] Bare substrate no oxidized, [b] Pre-oxidized (2 min. at 700°C dry air), [c] 800°C and 0% of Relative Humidity, [d] 800°C and 10% of Relative Humidity.

Table 8. Weight percent content of the 316L bare substrates with no coating after different oxidation conditions.

	Weight %				
	Fe	Cr	Ni	Si	O
(a) Bare substrate no oxidized	72.66	16.39	10.33	0.61	--
(b) Pre-oxidize substrate	71.96	17.02	10.28	0.620	0.12
(c) Bare substrate 800C RH-0%	64.04	26.61	5.8	1.15	2.40
(d) Bare substrate 800C RH-10%	61.06	30.0	4.68	1.31	2.95

In the Figure 27, a series of coated samples with low to high content of colloidal dispersion CeO_2 coating illustrates the surface topographies of the films deposited. The Figure 27 (a) shows the characteristic presence of droplets with spherical shape from 3 to 20 microns in diameter and the low weight content of

Ce (3.04 weight %). In Figure 27 (b), (c), (d) and (f) the deposited film is characterized by irregularly shaped polycrystalline grains with varying dimensions and cracks, the colloidal dispersion of cerium oxide in acetic acid (2.5%) provide this anomaly. However, at lower concentration of 2.5% rate of acetic acid the mean average size of nanocrystalline grains of CeO_2 is observed to increase and at lower concentration of acetic acid the corrosion resistance of the nano cerium oxide films decrease. In Figure 28 (c) and (d) shows a moderate-high weights content of Ce (4.12 to 4.22 weight %). In Figure 28 (e) and (f) shows an adequate high weights percent concentration of Ce (51.3 to 54.2 weight %), providing the highest oxidation protection resistant coating, with slight difference of Ce content in the cracks and the coat. As the Ce content increase, the presence of Fe and Cr diminish, as shown in Table 9.
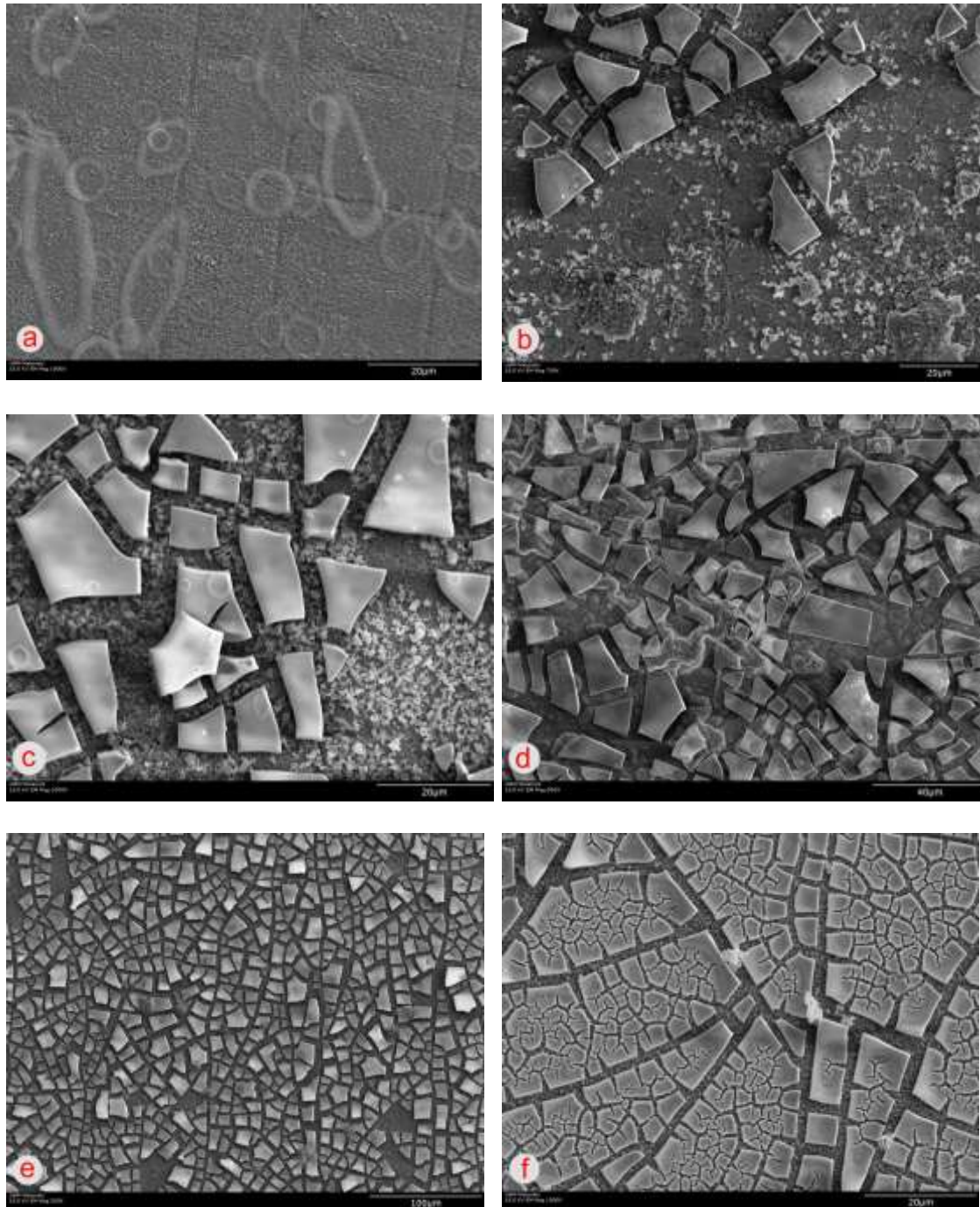
Figure 27. SEM micrographs, different weight content of ceria coating (a) Very low content, 1000x (b) Low content, 700x, (c) Moderate-high content, 500x (d) Moderate-high content, 1000x (e) High content, 200x (f) High content, 500x.
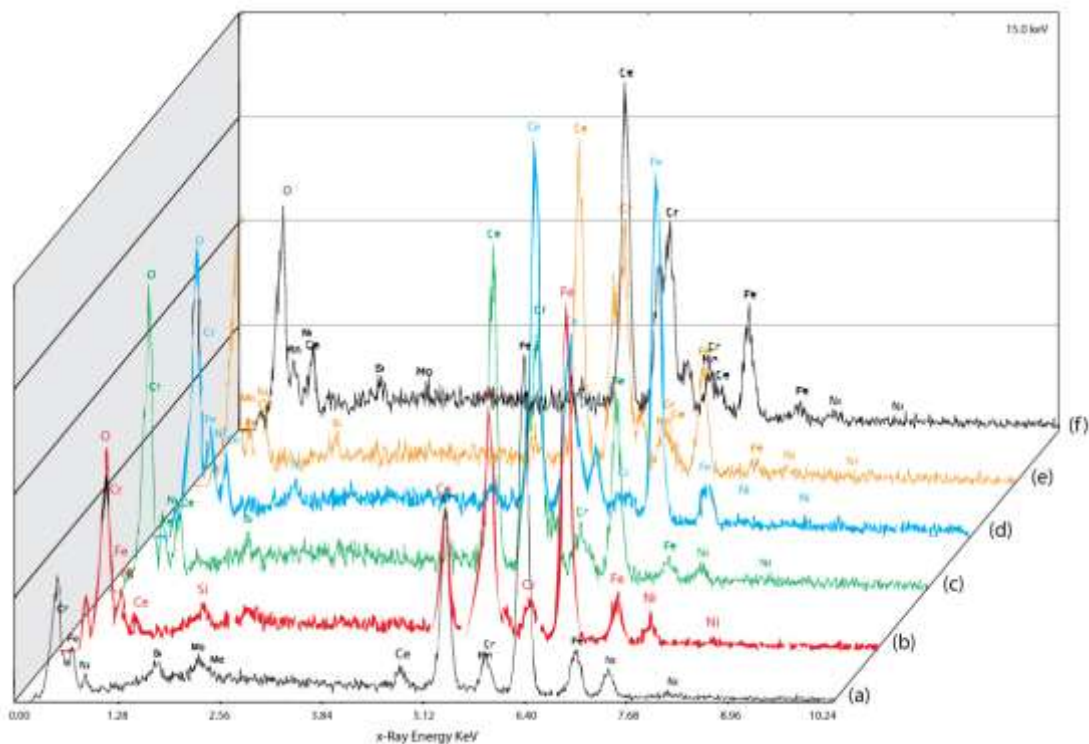
Figure 28. EDS spectrum analysis, different weight content of ceria coating (a) Very low content (b) Low content (c) Moderate-high content (d) Moderate-high content (e) High content (f) High content.

Table 9. Average weight percent content of the coated substrates from low to high content of ceria after different oxidation conditions.

	Weight % (Approximate)							
	Ce	Fe	Cr	Ni	Si	O	Mn	Mo
(a) Very Low content	3.4	55.5	24.4	9.1	0.7	2.8	1.8	2.2
(b) Low Content	15.4	53.8	19.7	3.1	0.9	3.4	1.9	1.8
(c) Mod-High Content	41.2	27.3	21.5	2.1	1.0	3.9	2.2	0.8
(d) Mod-High Content	42.2	28.8	20.1	2.2	0.8	3.9	1.3	0.7
(e) High Content	51.3	19.1	21.8	1.9	0.4	4.2	1.2	--
(f) High Content	54.2	18.9	18.3	2.0	--	4.1	1.9	0.7

4.6. XRD - High Temperature Oxidation Characterization

A double angle XRD with unresolved Cu Kλ radiation is used in this characterization in the 2Θ range of 20° to 75°, and high resolution scans to better determine the position of the principal peaks of the ceria films as well as the oxides formed on the substrate.

The Figure 29, shows the XRD spectrum for non-coated bare samples. The pre-oxidized sample was exposed for 2 minutes at 700ºC in dry air as pre-treatment prior to the coating deposition and shows characteristic peaks from the oxides: Fe_3O_4, NiO and Cr_2O_3. At 800ºC with 0% of relative humidity the presence of new peaks is observed which were identified as characteristics of $MnCr_2O_4$ spinel and Fe_2O_3. At 800ºC the effect of the 10% relative humidity increase the content of the spinel and Fe_2O_3.
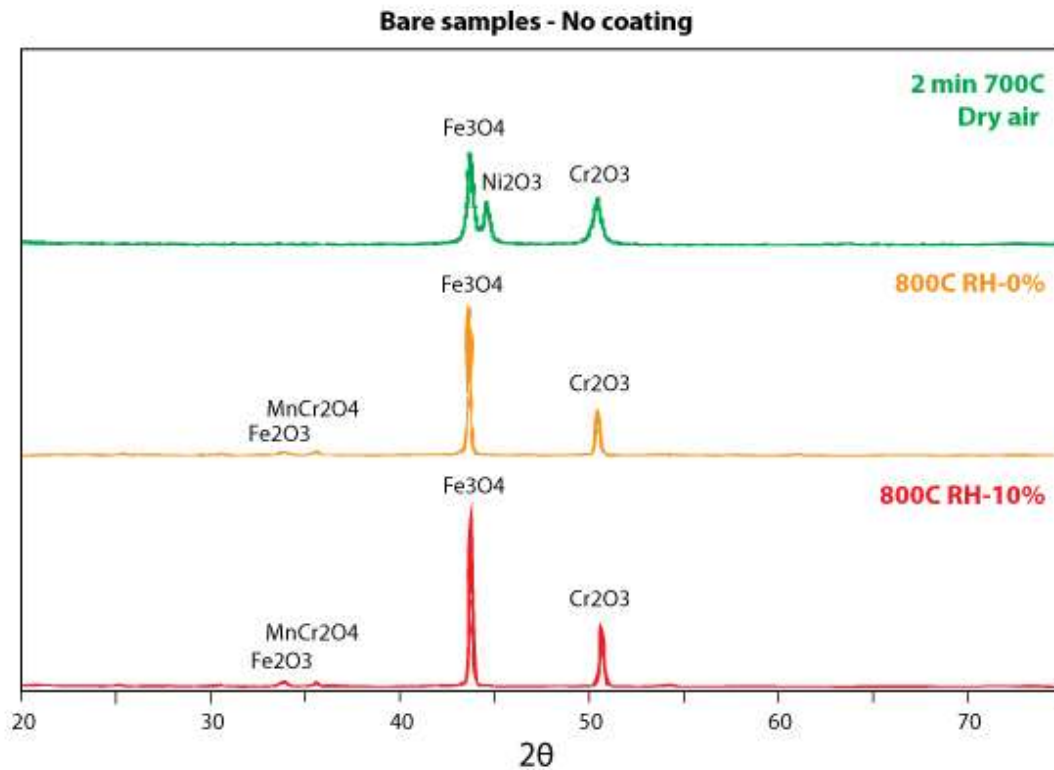
Figure 29. XRD spectrum for bare samples, pre-oxidized for 2 min. at 750℃, for 16 hrs at 800℃ with 0% RH and 16 hrs at 800℃ with 10% RH.

In the Figure 30, the coated samples are exposed to 750℃, 800℃ and 850℃ with 0% of relative humidity. The CeO_2 peaks are increasing with the change of temperature, and the characteristic peaks of Fe_3O_4 and Cr_2O_3 seem steady, the presence of CeO_2 at different angles is more notorious as the temperature increase.
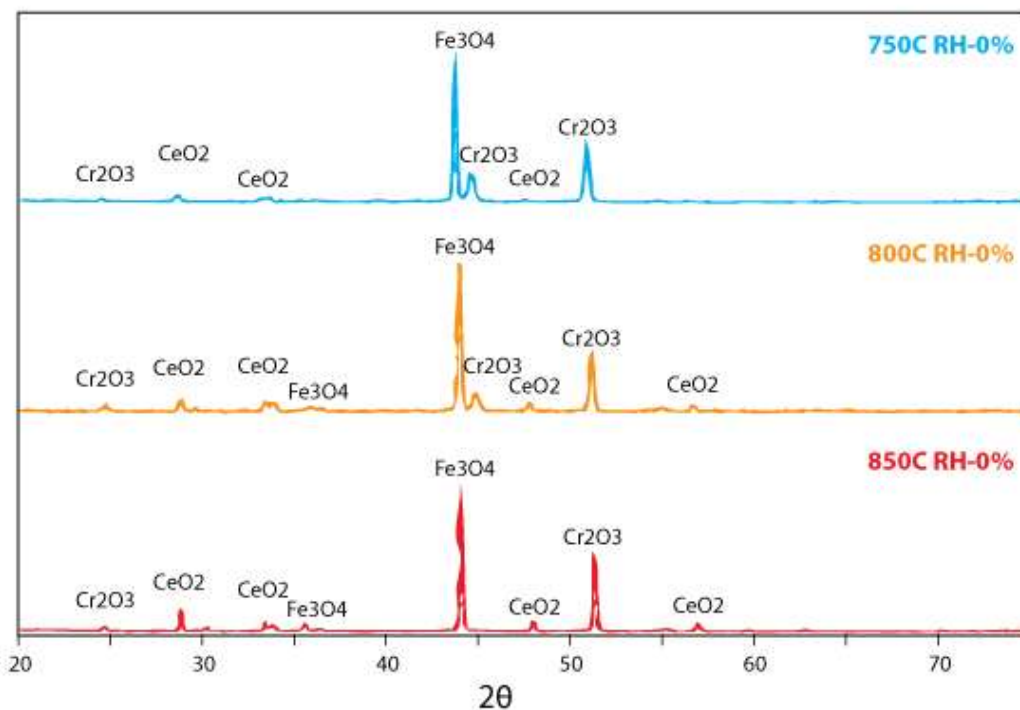
Figure 30. XRD spectrum for 750°C, 800°C and 850°C with 0% of relative humidity.
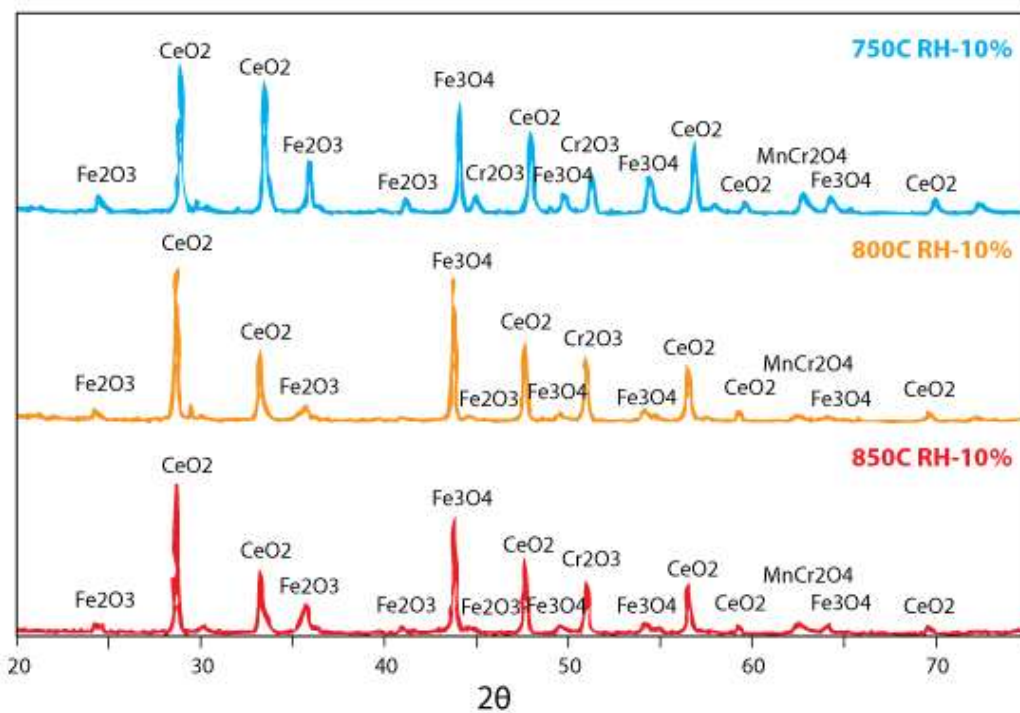
Figure 31. XRD spectrum for 750°C, 800°C and 850°C with 10% of relative humidity.
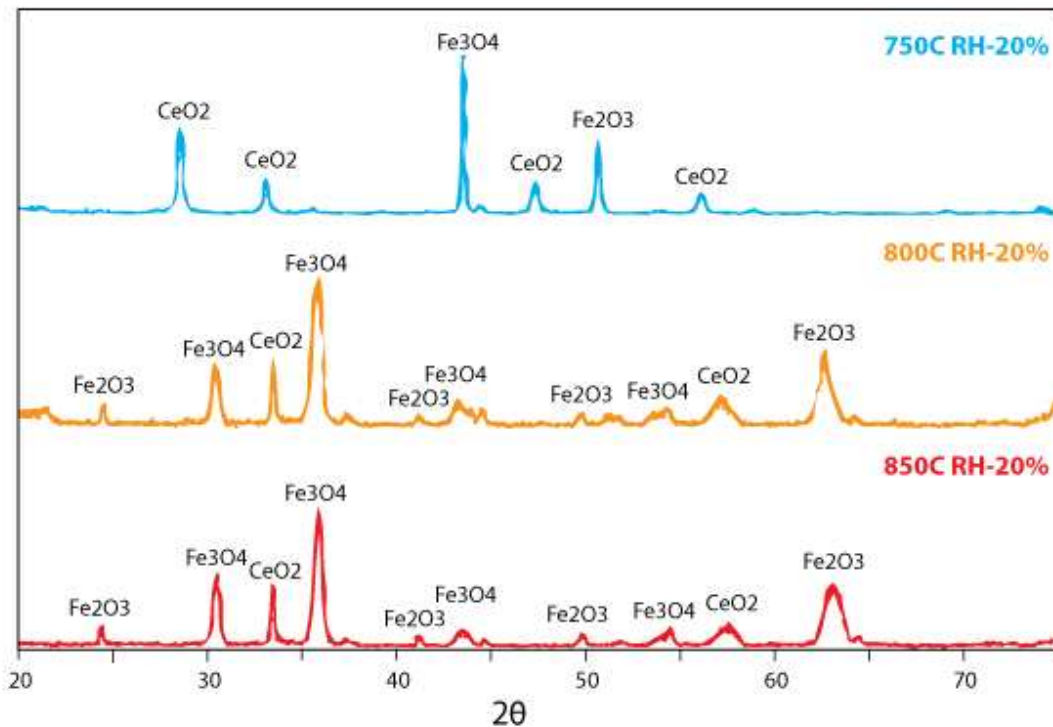
Figure 32. XRD spectrum for 750°C, 800°C and 850°C with 20% of relative humidity.

In the Figure 31, the coated samples are exposed to 750°C, 800°C and 850°C with 10% of relative humidity. The increasing presence of CeO_2 and the low change of Fe_2O_3, Cr_2O_3, suggest that the oxidation effect in the substrate has been minimized, and the CeO_2 is acting as a protective coating. In the Figure 32, the coated samples are exposed to 750°C, 800°C and 850°C with 20% of relative humidity. The increment of Fe_3O_4 peaks are related to the loss of protective coating, it seems that at a higher content of relative humidity the coating may loss adhesion with the substrate.

5.   DISCUSSION

Cerium oxide coatings applied to an austenitic stainless steel have been shown to provide a benefit to oxidation performance over a range of temperatures and humidity levels. The benefits of the cerium oxide in dry air was shown previously [10], but the performance as a function of humidity in the test environment remained to be shown. The inclusion of humidity in the test is critical for expansion of this potential method for creating longer-lasting materials in many important engineering applications. One example is the heat exchangers used in steam based power generation units which tend to include significant amounts of austenitic stainless steel. The testing done here was of modest duration (16 hours) compared to the desired lifetimes of power gen components (10+ years). Additional long term tests will need to be conducted to verify long term performance.

The particle size and homogeneous dispersion of cerium oxide has an important role in the coating deposition. The stability of the solution of 20 wt. % colloidal dispersion of Cerium Oxide (CeO_2) in 2.5% of acetic acid with an average of 19 nm of particle size, is considered ideal for a steady concentration of CeO_2 in the film coating. Previously, a solution of Cerium Oxide with 10 wt. % disperse in water with a 10nm of particle size has been used as coating [10]. Showing a high degree of agglomeration of the particle size, as an effect of the pH in the zeta potential. Therefore, the concentration of the cerium content on the

coating fluctuates detrimentally with the use of the cerium oxide solution disperse in water.

However, the colloidal dispersion solution of cerium oxide in acetic acid has a steady average particle size with no agglomeration. The downside of this solution is the non-uniform film deposited through the spraying method, being characterized by well defined irregularly shaphed polycrystalline grains with a cracked surface. Obtaining coating films up to 52% of weight content of CeO_2.

The oxide analysis at 20% of relative humidity has been affected during the process of preparation and mounting of the samples in the XRD. After the exposure to the isothermal conditions at 20% of relative humidity, the cerium oxide coating may decrease the adhesion forces with the substrate. The preparation of the samples for the XRD analysis, involve to cut the samples at least on half (20 mm x 15 mm) approximately. During the manipulation of the samples was noticed that coating fell off. This effect must be confirmed with further testing, with exposure to higher humidity levels and to longer periods of time, in order to confirm this effect.

The experimental set up of the unit control of the relative humidity has shown some challenges. During the enriched oxygen air flow containing 10% and 20% of relative humidity, the heating tapes situated by the connection between the lower inlet of the TGA and the evaporator were of limited lifetime affecting the constant flow of the humidity level. There is a need to improve this

aspect of the experimental set-up such that accurate test atmospheres that are dependable over long periods can be achieved.

Both solutions show low adherence to the substrate. Low interfacial intermolecular interaction between Austenitic stainless steel 316L and the two different solutions of cerium oxide has been noted through the easiness to remove the coating using solvents such as acetone and MEK, prior to the isothermal treatment. Cerium has been applied in low contents (0.5%), by the pack-cementation process, using a pack mixture containing Al, Si, NH_4Cl and Al_2O_3 [25]. However, the adhesion of the deposition has not been reported. Cerium mixtures enhancing the adhesion without compromising the coating and particle size is been considered. All coating systems are liable to fail eventually. But, the development of a proper coating deposition method can result in a beneficial life-time for the coating. Future work to improve the adhesive forces is strongly considered.

6.   CONCLUSIONS

The use of cerium oxide as anticorrosion coating with extended durability for steel protection in harsh environments was investigated under a range of temperatures and humidity levels. The following conclusions can be drawn from the results of this work:

- The oxidation of 316L substrates with ceria coating were investigated in dry and humid environments at 750°C, 800°C and 850°C with 0%, 10% and 20% of humidity levels.

- Cerium oxides coating may prevent crevice corrosion and increase pitting resistance of 316L relative to the uncoated substrate at high temperatures and different levels of relative humidity acting as a protective oxidation barrier.

- The parabolic rate constant is affected by the temperature and humidity levels; and this dependence is represented by the Arrhenius equation.

- The experimental determination of the activation energy, E_a, for 0%, 10% and 20% of relative humidity is calculated from the plot of ln kp vs. 1/T as a straight line, measuring the slope of E_a/R (where R is the gas constant) using the 3 different temperatures were the CeO_2 coating has been thermogravimetric analyzed.

- The oxidation kinetics of the cerium oxide coating follows a parabolic rate. The coated sample at 0% and 10% of relative humidity exhibited a

parabolic oxidation rate. For the samples at 20% shows a tendency of parabolic to linear oxidation behavior as a function of the temperature.

- The calculated parabolic rate constants Kp, at the experimental temperatures tend to increase as a function of humidity levels.

- The activation energy tends to increase proportionally to higher level of humidity exposures.

- At 0% relative humidity a value of 319.29 K J/mol of activation energy is being obtained and at 20% is 366.10 KJ/mol. For the 10% an approximate value of 343.00 KJ/mol has been estimated based on the projection of the kp the values at 750°C and 800°C.

- The coatings with 0% exposure of relative humidity exhibit the lowest overall weight gains.

- The oxygen and cerium content can reach richer concentration as the uniformity of the films is attained as shown in the Table 9.

- At 10% of relative humidity the formation of CeO_2 and Fe_3O_4 is more predominant than samples at 0% of relative humidity.

- The presence of the CeO_2 coating, reduced the oxidation kinetics and provided good cyclic oxidation resistance at increments of relative humidity.

FUTURE WORK

- The unit control of relative humidity plays a key role in the performance of the CeO2 coatings for this project, developing or obtaining a unit with higher reliability is critical.

- Apply alternatives methods for coating deposition:

  - Plasma spray-physical vapor deposition.

  - Thermal Spraying.

  - Pack cementation.

- Developing a method to control a precise thickness of nanofilm coatings.

- Improving the adhesion between SS 316L substrate and CeO_2 coatings.

- The use of different substrates such aluminum alloys.

- Cross sectional SEM studies should be conducted to verify the thickness and composition of the different weigh contents.

REFERENCES

[1]   J. Antill, K. Peakball, Influence of an alloy addition of Yttrium on the oxidation behavior of austenitic SS and FSS in 1 temperature oxidation for chromium. Corros. Sci. 1972; 12:265.

[2]   L. Tye and N. A. El-Masry, Applied Physics Letters Vol. 65, p. 3081 (1994).

[3]   P. Kofstad, High-Temperature Oxidation of Metals, p.112.

[4]   National Academy of Sciences/ National Academy of Engineering, High-Temperature Oxidation-Resistant Coatings, 1970, p. 22.

[5]   C. Wagner, J. Electrochem Soc. 99, 1952 p.369

[6]   P. Kofstad, High Temperature Corrosion, Elsevier, London, 1988, p. 1-558.

[7]   S. Elliot, The Physics and Chemistry of Solids, John Wiley & Sons, Chichester, England, 1998, p. 1-772.

[8]   L. Mikkelsen, High Temperature Oxidation of Iron-Chromium Alloys,. www.risoe.dk/rispubl/reports/ris-phd-2.pdf

[9]   B. Pieraggi, Calculations of Parabolic Reaction Rate Constants. Oxidation of Metals, Vol. 27, Issues 3-4, p. 177-185, April 1987.

[10]   H. Mendoza, High Temperature Stability of a 316 austenitic stainless steel coated with CeO2 Nanoparticles.

[11]   D. Ocepek, Mechanical Process Technology, 1989.

[12]   B. Salopek, D. Krasic, S. Filipovic, Measurement and Application of Zeta-Potential. Rudarsko-geolosko-naftni zbornik, Vol. 4, p. 147-151.

[13]   R. Hunter, Zeta Potential in Colloid Science: Principles and Applications, 1988, Academic Press, UK.

[14]   T. Zhang, D. Tang, Current Research Status of Corrosion Resistant Coatings. Recent Patents on Corrosion Science, 2009, 1, 1-5.

[15]   C. R. Hammond (2000). The Elements in Handbook of Chemistry and Physics 81st edition, CRC press.

[16]   Patnaik, Pradyot (2003). Handbook of Inorganic Chemical Compounds. McGraw-Hill. p. 199-200.

[17]   Lavik, E. B.; Chiang, Y.M. Material Research Society Symposium Proceeding 1997, 457, 63-68.

[18]   Mogensen, M.; Sammes, S. M.; Tompsett, G. A. Solid State Ionics 2000, 129, 63-94.

[19]   Bamwenda, G. R.; Arawaka, H. Journal of Molecular Catalysis A. Chemical 2000, 161, 105-113.

[20]   A. Catalysis Reviews: Science and Engineering. 1996, 38, 439-520.

[21]   C. J. Patridge.   Rare-earth oxide ceramics found to be robustly hydrophobic. Cambridge University Press. MRS Bulletin, Volume 38, April 2013, p. 295.

[22]   H. Hasannejad, T. Shahrabi, M. Aliofkhazraei, Effects of Acetic Acid on Microstructure and Electrochemical properties of Nano Cerium Oxide Films Coated on AA7020-T6 Aluminum Alloy.

[23]   D.R.Gabe, Principles of metal surface treatment and protection. 1972, p. 69.

[24] G. Haugstad, Atomic Force Microscopy: Understanding basic modes and advanced applications. 2012, Published by John Wiley & Sons, Inc.

[25] A. Ali, M. Khedeir, R. Mohammed, Improving Oxidation Resistance of Stainless Steel (AISI 316L) by Pack Cementation. Eng. and Technology, Vol. 25, No. 7, 2007.